



12-2013

# Reconstruction of Patient-Specific Bone Models from X-Ray Radiography

Hatem Amin Abdel Fattah El Dakhakhni  
*University of Tennessee - Knoxville, heldakha@utk.edu*

---

## Recommended Citation

El Dakhakhni, Hatem Amin Abdel Fattah, "Reconstruction of Patient-Specific Bone Models from X-Ray Radiography." PhD diss., University of Tennessee, 2013.  
[https://trace.tennessee.edu/utk\\_graddiss/2568](https://trace.tennessee.edu/utk_graddiss/2568)

This Dissertation is brought to you for free and open access by the Graduate School at Trace: Tennessee Research and Creative Exchange. It has been accepted for inclusion in Doctoral Dissertations by an authorized administrator of Trace: Tennessee Research and Creative Exchange. For more information, please contact [trace@utk.edu](mailto:trace@utk.edu).

To the Graduate Council:

I am submitting herewith a dissertation written by Hatem Amin Abdel Fattah El Dakhakhni entitled "Reconstruction of Patient-Specific Bone Models from X-Ray Radiography." I have examined the final electronic copy of this dissertation for form and content and recommend that it be accepted in partial fulfillment of the requirements for the degree of Doctor of Philosophy, with a major in Biomedical Engineering.

Mohamed R. Mahfouz, Major Professor

We have read this dissertation and recommend its acceptance:

Richard D. Komistek, Aly E. Fathy, William R. Hamel

Accepted for the Council:

Carolyn R. Hodges

Vice Provost and Dean of the Graduate School

(Original signatures are on file with official student records.)

---

# Reconstruction of Patient-Specific Bone Models from X-Ray Radiography

A Dissertation Presented for the  
Doctor of Philosophy  
Degree  
The University of Tennessee, Knoxville

Hatem Amin Abdel Fattah El Dakhakhni  
December 2013

Copyright © 2013 by Hatem El Dakhkhni

All rights reserved.

To my father

*Amin El Dakhkhni*

## Acknowledgements

---

I would like to thank my advisor and mentor Dr. Mohamed Mahfouz for his constant support of my research and career goals. With the guidance of Dr. Mahfouz, I have been able to gain valuable technical and life skills that will remain with me all the way through my future. His ambition, persistence, motivation, and hard work were, and will always be, an inspiration. The journey we had together was a lifetime experience that shaped who I am today.

I would like to thank my advisory committee Dr. William Hamel, Dr. Richard Komistek, and Dr. Aly Fathy, in conjunction with Dr. Mahfouz for sharing their technical and life expertise, to guide me through my research and career planning.

I would like to thank my fellow graduate students at the Center of Musculoskeletal Research, who paved the way for my research, and walked with me through the journey including Dr. Michael Kuhn, Dr. Brandon Merkl, Dr. Gary To, Dr. Emam Fatah, Dr. Rimon Tadross, Dr. Michael Johnson, Dr. Joseph Mitchell, Dr. Emily Pritchard, Lyndsay Bowers, Wesley Underwood, Jing Wu, Rebecca Robertson and all the wonderful team for their support over the years.

I would like to thank my friends that supported me through my highs and lows, and finally pushed me through to graduation, especially Ali and Nada Mustafa, Anis and Layla Abaab, Essam and Dounia ElKhouly, Marouane and Habiba Salhi, Yassin and Tamara Tero, Enas Wahdan, and Ola Sweif.

Finally, I would like to thank my parents and siblings, whose love and support kept me going through all the tough times.

## Abstract

---

The availability of a patient-specific bone model has become an increasingly invaluable addition to orthopedic case evaluation and planning [1]. Utilized within a wide range of specialized visualization and analysis tools, such models provide unprecedented wealth of bone shape information previously unattainable using traditional radiographic imaging [2]. In this work, a novel bone reconstruction method from two or more x-ray images is described. This method is superior to previous attempts in terms of accuracy and repeatability. The new technique accurately models the radiological scene in a way that eliminates the need for expensive multi-planar radiographic imaging systems. It is also flexible enough to allow for both short and long film imaging using standard radiological protocols, which makes the technology easily utilized in standard clinical setups.

# Table of Contents

---

<b>Chapter 1: Motivation and Background</b> .....	<b>1</b>
<b>1.1 Motivation</b> .....	<b>1</b>
<b>1.2 Background</b> .....	<b>5</b>
1.2.1 Template Model .....	6
1.2.2 Feature Extraction .....	7
1.2.3 Registration .....	9
1.2.4 Template Morphing .....	10
1.2.5 Overview .....	11
<b>1.3 Contributions</b> .....	<b>14</b>
<b>1.4 Organization</b> .....	<b>15</b>
<b>Chapter 2: Materials and Methods</b> .....	<b>16</b>
<b>2.1. Imaging and Preprocessing</b> .....	<b>16</b>
<b>2.2. Bone Shape Modeling</b> .....	<b>19</b>
2.2.1 Bone Model Dataset.....	21
2.2.2 Template Bone .....	22
2.2.3 Model Fitting.....	23
2.2.4 Template Warping and Correspondence Matching .....	25
2.2.5 Partial Bone Generation and Alignment .....	27
2.2.6 Decoupling of Scale from the Statistical Shape Model .....	28
2.2.7 Atlas Generation .....	29
<b>2.3. Feature Extraction</b> .....	<b>29</b>
2.3.1. Manual Segmentation .....	34
2.3.2. Automatic Segmentation .....	35
<b>2.4 Registration</b> .....	<b>40</b>
2.4.1 Radiological Scene Simulation.....	42
2.4.2 Calibration Target Pose Extraction .....	44
2.4.3. Model Rotational Pose Estimation .....	50
2.4.4 Scale initialization.....	75



<b>2.5. Model Deformation .....</b>	<b>76</b>
2.5.1. Build 3D Simulated Scene.....	76
2.5.2. Model Point selection .....	77
2.5.3. Calculation of 3D Displacement Vectors .....	79
2.5.4. Deformation Using Projection on Convex Sets (POCS) .....	80
2.5.5 Cartilage Estimation .....	85
<b>Chapter 3: Verification and Results.....</b>	<b>86</b>
<b>3.1 Fitting RMS Error Assessment .....</b>	<b>86</b>
<b>3.2 Mechanical Axis Calculation Accuracy Assessment .....</b>	<b>89</b>
<b>3.3 Femur Reconstruction .....</b>	<b>94</b>
<b>3.4 Tibia Reconstruction .....</b>	<b>96</b>
<b>References.....</b>	<b>98</b>
<b>Vita .....</b>	<b>104</b>

## List of Tables

---

Table 1 Comparison of model reconstruction using different imaging modalities. ....	4
Table 2 Number of bones used to create the relevant gender-specific atlases. ....	21
Table 3 Analogy between x-ray radiography and perspective imaging.....	43
Table 4 Fitting RMSE between femur x-ray reconstructions utilizing the scale independent atlas and manual segmentations. ....	88
Table 5 Fitting Root Mean Square Error between tibia x-ray reconstructions utilizing the scale independent atlas and manual segmentations. ....	88
Table 6 Femur Mechanical accuracy assessment compared to MRI .....	92
Table 7 Tibia Mechanical accuracy assessment compared to MRI .....	93
Table 8. Mean Femur RMS error and STD for reconstructions .....	94
Table 9. Mean Tibia RMS error and STD for reconstructions.....	96

## List of Figures

---

Figure 1 Examples of 3D analysis tools. Top left: surgical planning. Top right: implant design. Bottom left: bone measurements. Bottom right: surgical jig design.....	2
Figure 2 Image slice showing 2D segmentation of a femoral cross section.....	3
Figure 3 3D MRI segmentation. ....	3
Figure 4 Block diagram of the workflow of bone model reconstruction from x-ray radiographs.....	5
Figure 5 Example of template models. Left: generic bone segmentation. Right: mean model for a bone dataset.	6
Figure 6 Example of extracted features. Top left: original femur in anterior-posterior (AP) view. Top right: original femur in lateral view. Bottom Left: Segmented AP image with the outer contour area shaded in red and internal contour defined in blue. Bottom Right: Segmented LAAT view with the outer contour area shaded in red and internal contours defined in blue and yellow .....	8
Figure 7 Example for a long-film case showing the AP view (left) and LAT view (right).....	17
Figure 8 Example showing how the AP view was divided into three images .....	18
Figure 9 Calibration target.....	18
Figure 10 Calibration target attached to leg.....	19
Figure 11 Statistical shape modelling process .....	20
Figure 12 Template models. ....	22
Figure 13 Image showing fitting steps between template model (purple) and high resolution model (pink). From left to right: principle axis alignment, scaling, and centroid alignment. ....	24
Figure 14 Image showing different pose initializations between template model (purple) and high resolution model (pink). ....	24
Figure 15 Images showing a distance map between the template and high resolution model after ICP alignment in mm. ....	25
Figure 16 Mutual correspondence warping. Copied from [31]. ....	26
Figure 17 Images showing a distance map between the template and high resolution model after template warping in mm.....	26
Figure 18 Partial bone extraction.....	27
Figure 19 Template distal femur shown in transparency mode (top) and candidate contour features highlighted in red (bottom). ....	30
Figure 20 Template proximal tibia shown in transparency mode (top) and candidate contour features highlighted in red (bottom). ....	31
Figure 21 Case 1. Original images (top) and candidate internal contours highlighted in red (bottom). ....	32
Figure 22 Case 2. Original images (top) and candidate internal contours highlighted in red (bottom). ....	33

Figure 23: Manual image segmentation (left) and segmented image (right). .....	34
Figure 24 Image showing the segmented outer contour shaded in red with the internal contours manually selected. ....	35
Figure 25 2D contour atlas creation flowchart. ....	36
Figure 26 Image showing synthetic image samples. ....	36
Figure 27 Initialized bone contour. ....	37
Figure 28 Contour fitting flowchart.....	38
Figure 29 Edge detection. Profile signal (left) and profile gradient (right) showing the detected profile edge point index, Pmax. ....	38
Figure 30 Image showing the fitting progress. The red contour represents the initial registered contour. Green points are edge points detected using the Savitzky-Golay filter. Blue points represent the contour after projecting back to the atlas. ....	39
Figure 31 Final segmentation results. ....	39
Figure 32 Projection model of the radiographic scene.....	41
Figure 33 Plot showing magnification trend as SID and OID change.....	41
Figure 34 PMF vs. object-to-image distance for a constant SID.....	42
Figure 35 Radiograph of the leg with the calibration target attached. ....	45
Figure 36 Multilevel Thresholding applied on x-ray image to extract beads.....	46
Figure 37 Extracted Beads .....	47
Figure 38 Semi-automatic brace initial placement to establish bead correspondences .....	48
Figure 39 Image showing a distal femur contour with the centroid marked in red, and the arrow highlighting the centroid distance .....	54
Figure 40 Graph showing the centroid distance function.....	54
Figure 41 Graph showing the repeated centroid distance function to be used in Fourier analysis .....	55
Figure 42 Fourier spectrum of the centroid distance function, showing the cutoff frequency used to select the sampling frequency.....	55
Figure 43: Flowchart showing contour region extraction and Identification.....	57
Figure 44: Proximal femur contour showing regions defined based on inflection points. The color of the contour points indicate their curvature. ....	59
Figure 45: Noise inflection points on femur contour .....	60
Figure 46: Femur contour smoothed at different Gaussian variances showing inflection points in green. ....	61
Figure 47: Curvature Scale Space representation of a femur bone showing different smoothing levels inflections .....	63
Figure 48: Region filtering effect.....	65
Figure 49: Labeled Contour Regions. Right: Proximal Femur. Left: Distal Femur .....	66

Figure 50 Image showing how some features are described.....	68
Figure 51 Origin point (Red) extracted using extracted features.....	73
Figure 52 Top: Corresponding origin points on the AP and LAT images. Bottom: Initialized bone placement in green. ....	74
Figure 53 Top: Before scaling, Bottom: After scaling .....	75
Figure 54: Block Diagram for the bone morphing process .....	76
Figure 55 Image showing 3D mapping of an image contour point. The red line is an example ray joining a contour point to the x-ray source location. The bead on the red line is the closest line point to the 3D model, and the shortest distance between the bead and the model indicates the 3D fitting error. ....	77
Figure 56 Left: Distance selection criterion. Right: Angle selection criterion .....	78
Figure 57 Model point selection. Alpha points (yellow) and distance points (blue). Intersection is in red. Here $\alpha = 10$ degrees, $d = 5$ mm. ....	79
Figure 58 Images showing POCS convergence. Left: If the two sets intersect, the convergence is to an intersection point. Right: if the two sets do not intersect, convergence is to a limit cycle that minimizes the distance between the two sets. From [52] .....	82
Figure 59 Image showing alternating projections. Right: Deformed bone after projecting onto the set <i>B</i> . Left: Same bone after projecting back to set <i>A</i> . ....	83
Figure 60 Thickness distance map of added cartilage. Top: Femur, Bottom: Tibia .....	85
Figure 61 Top: X-ray images with the reconstructed bone projected. Bottom: Reconstructed 3D model showing beads representing x-ray extracted 3D fitting points. The colormap on the bone shows the distance to the beads in cm.....	87
Figure 62 EAP Calculation. Top: Femoral Head center. Bottom: Ankle Center .....	89
Figure 63 2D and 3D mechanical axis angular error calculation .....	91
Figure 64. Distal Femur surface distance map between x-ray reconstruction and manual MRI segmentation for the live patient. Right: With estimated cartilage, Left: Without estimated cartilage. Positive values indicate the x-ray reconstruction is larger than the manual segmentation, negative values indicate smaller regions. ....	95
Figure 65. Proximal tibia surface distance map between x-ray reconstruction and manual MRI segmentation for the live patient. Right: With estimated cartilage, Left: Without estimated cartilage. Positive values indicate the x-ray reconstruction is larger than the manual segmentation, negative values indicate smaller regions. ....	97

## Scientific Terminology

---

cm	Centimeter
Hz	Hertz
mm	Millimeter
mSv	Millisievert

## Acronyms

---

1D	One Dimensional
2D	Two Dimensional
3D	Three Dimensional
C++	C Plus Plus software language
CT	Computed Tomography
EAP	Extreme Mechanical Axis Points
GUI	Graphical User Interface
ICP	Iterative Closest Point
MRI	Magnetic Resonance Imaging
OID	Object-to-Image Distance
PMF	Projective Magnification Factor

RMS	Root Mean Square
RMSE	Root Mean Square Error
Rx	Rotation around the x-axis
Ry	Rotation around the y-axis
Rz	Rotation around the z-axis
SID	Source-to-Image Distance
SNR	Signal-to-Noise Ratio
SOD	Source-to-Object Distance
SSM	Statistical Shape Model
TKA	Total Knee Arthroplasty
Tx	Translation in the X-Direction
Ty	Translation in the Y-Direction
Tz	Translation in the Z-Direction

# Chapter 1: Motivation and Background

---

## 1.1 Motivation

X-ray radiography is the historical medical standard imaging modality for orthopedic diagnosis. It provides an excellent insight into the global shape of bones, which makes it possible, for example, to detect fractures, deformities, and assess joint health. It also has the advantages of low cost, portability, unique imaging speed, very low ionizing radiation (as compared to CT), and no hazard risk to patients with ferromagnetic implants (as compared to traditional MRI machines). Orthopedic case evaluation and surgical planning traditionally relies on a small number of 2D x-ray radiographs for the extraction of anatomical information. Although this was proved to be sufficient for a subset of diagnostic procedures, quantitative analysis can suffer from inaccuracies and lack of information due to the projective imaging nature of x-ray radiography [3]. Drawbacks for which could include, but are not limited to, a combination of increased patient pain, surgical time and cost, and implant revisions.

With the tremendous advancement of imaging, computational, and visualization power, 3D bone shape analysis was introduced as a viable option for patient evaluation and treatment. Such an option is introduced by the generation of a patient-specific computerized bone model that comprises an accurate geometrical depiction of the patient's anatomy [1]. Utilized within a wide range of specialized visualization and analysis tools (Figure 1), such a model would provide unprecedented wealth of bone shape information and measurement accuracies previously unachieved within traditional radiographic imaging [2].



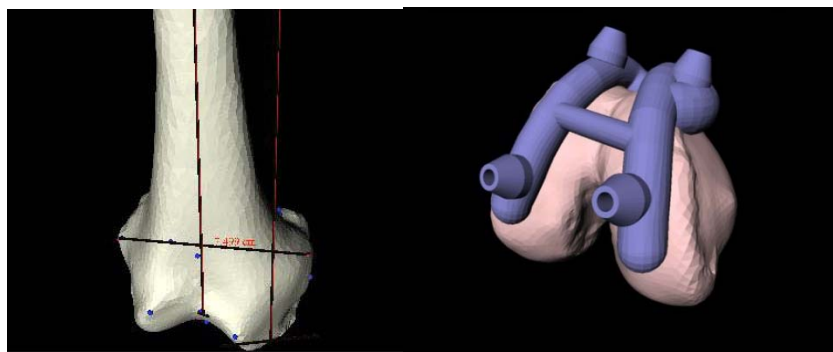
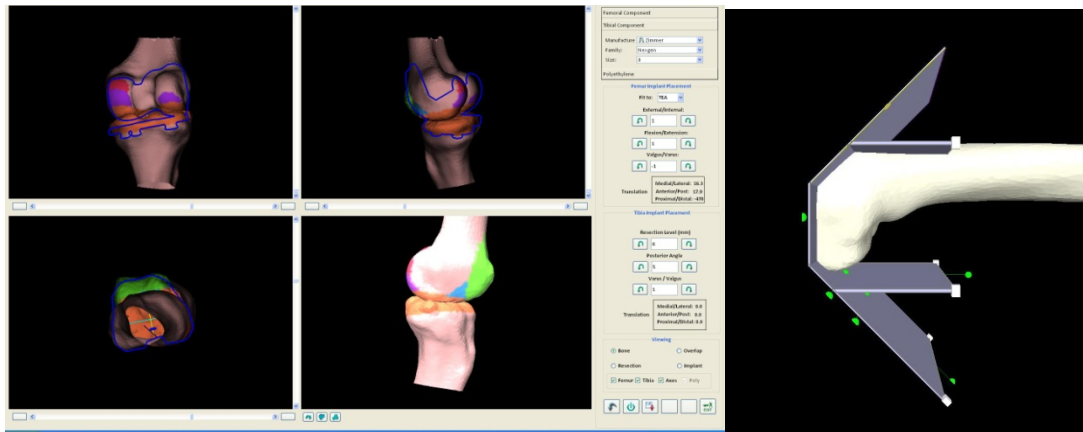


Figure 1 Examples of 3D analysis tools. Top left: surgical planning. Top right: implant design. Bottom left: bone measurements. Bottom right: surgical jig design.

Unfortunately, there have been limitations to the wide spread application of 3D analysis. These limitations are mainly due to the need for a volumetric imaging modality dataset to obtain such models, most commonly being CT or MRI. These volumetric imaging modalities provide datasets comprised of slices representing anatomical cross sections of the bone of interest. The slices can then be segmented individually (Figure 2) or collectively (Figure 3) to provide accurate patient-specific 3D bone models. The drawback is high imaging cost, which limits their utilization as compared to traditional radiography. Table 1 shows a brief comparison for knee bone model reconstruction using different imaging modalities.

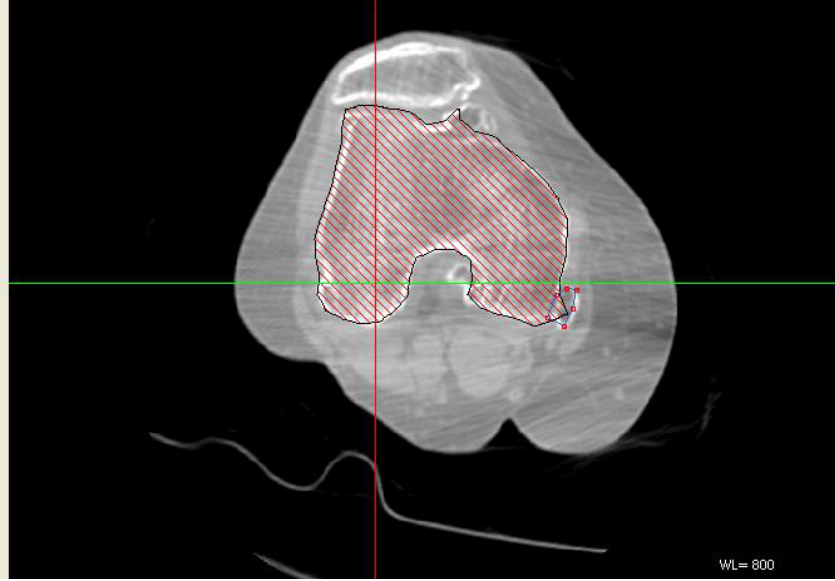


Figure 2 Image slice showing 2D segmentation of a femoral cross section.

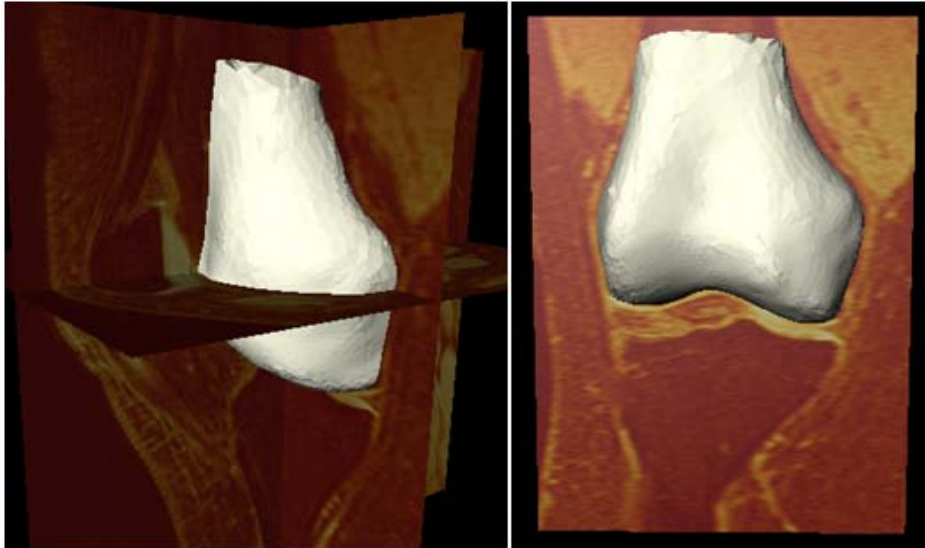


Figure 3 3D MRI segmentation.

**Table 1 Comparison of model reconstruction using different imaging modalities.**

	<b>MRI</b>	<b>CT</b>	<b>X-Ray</b>
Dimensionality	Volumetric (3D)	Volumetric (3D)	Projective (2D)
Number of Images	>400	>700	2 or more
Cartilage	Yes	No	No
Ionizing radiation	None	3-8 mSv	0.04 mSv
Cost (National Avg.)[4]	\$2500	\$1100	\$300
Processing time	1-4 hours	1-2 hours	<15 minutes

Furthermore, the time-consuming nature of the volumetric dataset imaging and segmentation process comprises a major bottleneck in industrial applications given the continuously increasing number of orthopedic surgery patients. To put this into perspective, the number of Total Knee Arthroplasties (TKAs) is expected to grow by 673% to 3.48 million procedures through 2030 [5].

The goal of this work is to utilize the low cost, widely available imaging provided by traditional radiography in a system that produces patient-specific bone models within an accuracy that is suitable for diagnosis and surgical planning. Processing time and system migration requirements were also taken into consideration, to insure maximum applicability and throughput.

## 1.2 Background

Researchers have made multiple attempts to generate patient-specific 3D bone models from a few (2 or more) x-ray images. In these attempts, the scarcity of image information due to the small number of images (compared to hundreds of images in the case of volumetric imaging) is compensated by the inclusion of prior information. This prior information is formulated to represent the bone's shape, in a way that allows for image feature guided model deformation. The hypothesis is that the image features, together with the prior shape information, constitute sufficient information from which the patient-specific anatomy could be recovered within the applications' accuracy requirements. Figure 4 shows a typical workflow for the bone reconstruction method from x-ray radiographs.

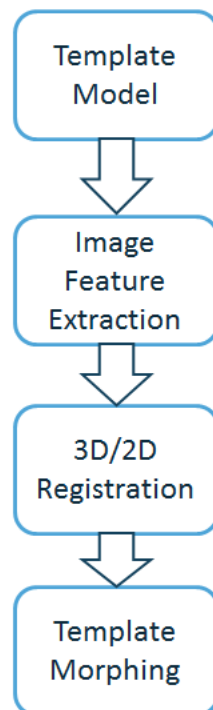


Figure 4 Block diagram of the workflow of bone model reconstruction from x-ray radiographs.

### 1.2.1 Template Model

The template model constitutes the bone-specific prior information, in the form of an initial shape estimate. The bone shape is represented in the form of a SSM, which can be obtained from either a 3D segmentation of a volumetric imaging dataset [6-8] or by calculating the statistical mean of a database of bone segmentations [9-12]. The model should be comprised of a number of vertices that is sufficient to accurately represent the bone anatomy detail and shape variation, while reducing storage and processing requirements. Figure 5 shows an example of the two template types. It can be noticed that the dataset mean provides a smoother initialization for reconstruction.



Figure 5 Example of template models. Left: generic bone segmentation. Right: mean model for a bone dataset.

In addition to providing an initial bone template, the bone dataset can also be used to obtain a shape's modes of variation by using Principle Component Analysis (PCA) [13]. This can be used in the morphing stage in a concise and anatomically-abiding deformation method.

### **1.2.2 Feature Extraction**

Image features are extracted information from the 2D radiographs that represent the anatomy of the imaged bone through its projection. They provide similarity measures that indicate the discrepancy between the 3D template bone model and the patient's anatomy. They also serve as a guide on how the template bone would need to be deformed in order to better represent the patient's bone. The extracted image features are normally limited to bone edges representing the bone surface's silhouette [7, 8, 11, 12, 14, 15]. Figure 6 shows an example of extracted features.

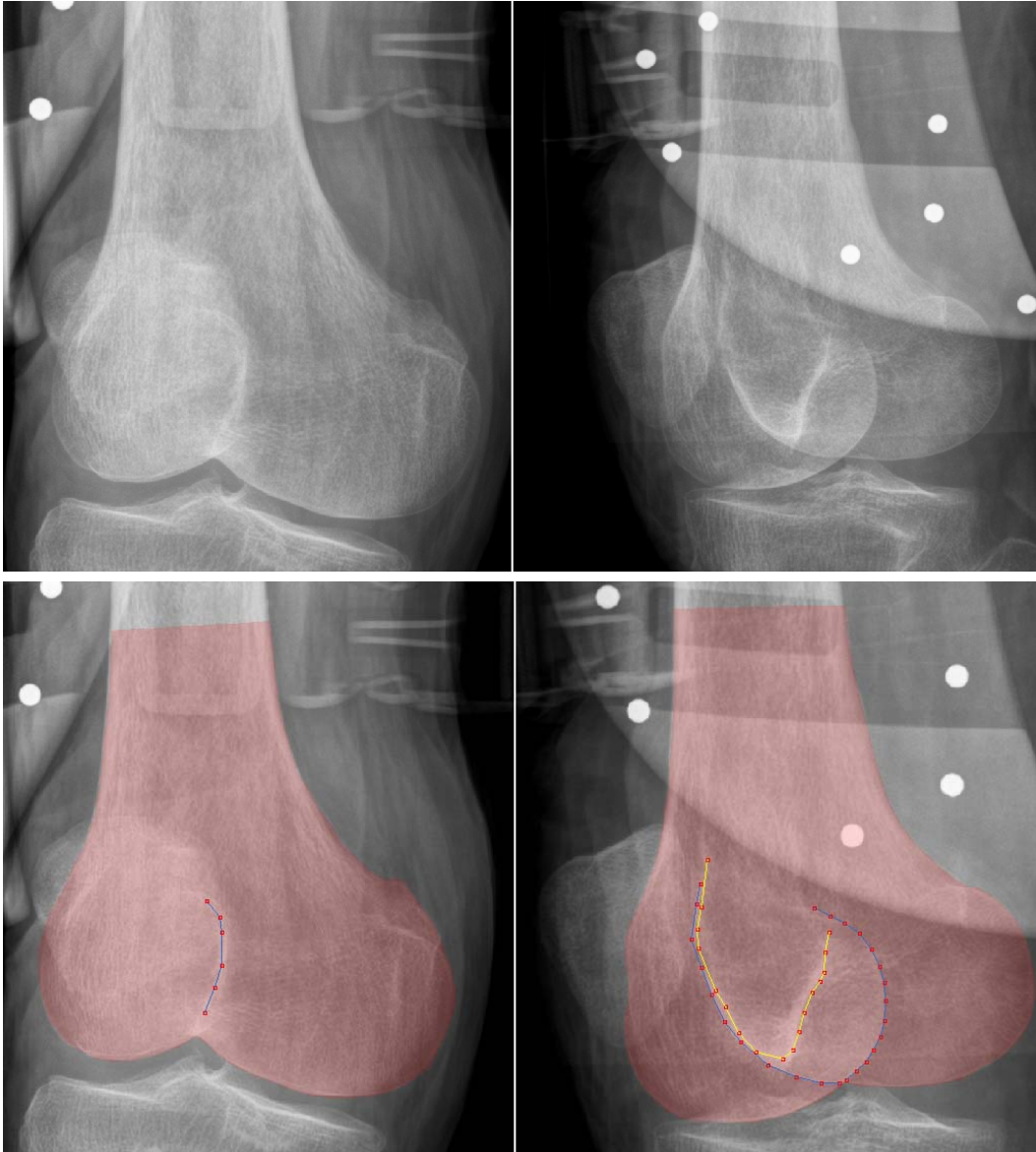


Figure 6 Example of extracted features. Top left: original femur in anterior-posterior (AP) view. Top right: original femur in lateral view. Bottom Left: Segmented AP image with the outer contour area shaded in red and internal contour defined in blue. Bottom Right: Segmented LAAT view with the outer contour area shaded in red and internal contours defined in blue and yellow

Feature extraction can be completed using three methods.

- a) Manually by selecting points defining the visible edges. If done by an expert, this is the least prone to errors; however, this process takes the most time to complete and is the most prone to user variability, especially in contour areas of low contrast [11].
- b) Automatically using an image processing edge detection algorithm such as the Canny edge detector [10-12, 16]. This is the most commonly used algorithm for surface reconstruction. It has the advantage of being completely automated but its main drawback is the dependence of the output on smoothing and thresholding parameters that need fine-tuning. This also makes the detection susceptible to false edges and discontinued contours, which could affect the reconstruction accuracy.
- c) Automatically using statistical shape/appearance models [13]. This method has the advantage of capturing the variation of contours using a learning dataset. It has the unique feature of estimating missing contour areas obtained by other methods and insuring the extracted contours comply with anatomical constraints.

### 1.2.3 Registration

Registration provides an affine transformation that would place the 3D template model in a location that mimics the original radiological setup. This allows the template to be directly matched and morphed in order to fit the extracted 2D features of the patient's radiographs. It represents an important initialization step that strongly impacts the outcome of bone reconstruction [17]. In [10], rib registration was completed using a crude and rigid registration



step that is based on manual 2D point/landmark matching. To minimize errors due to inaccurate registration, the authors sampled the registration space by a number of small steps around the initial estimate, performing bone optimization at each step. The sample that resulted in the minimum model perspective projection to image contour error was selected as the algorithm output. In [11, 18], an Iterative Closest point registration [19] was used to estimate the scale and rigid transformation of a template proximal femur to projection lines, which does not guarantee optimum pose extraction. In [12], the authors deal with the problem of a large amount of local minima by performing several conjugate gradient affine optimizations. This was done by adding small random displacements in the range of -10 to +10 mm/degrees to the previously known ground-truth pose. Other methods rely on manual landmark correspondence matching on different images for registration [7, 20]. These methods are prone to landmark definition inaccuracies due to the smooth nature of bone surfaces and the projective nature of x-ray imaging. They also require a constrained rotational setup between images, or that the images would be taken simultaneously. The latter would require biplanar imaging, an expensive alternative to traditional radiology that is not widely available in imaging facilities.

#### **1.2.4 Template Morphing**

Template morphing is a deformation stage that aims to minimize an error function formulated between the template model and detected image features by iteratively morphing the template bone. The methodology by which the template model is deformed is highly associated with how the template is formulated. Generic templates are morphed by moving control points on the surface of the template bone. After that, since the control points are

sparse relative to the amount of 3D deformation needed for shape integrity, missing data is usually estimated and smoothed out by an interpolation method such as Thin-Plate Splines [9], or Kriging [7, 20-23]. The major drawback for such deformation is that it does not necessarily follow anatomical shape variation constraints, which would make the reconstruction algorithm prone to producing unrealistic 3D models. Statistical models do not suffer from this drawback and, hence, have become the more popular templating method [10].

Morphing a template belonging to a statistical model is done by optimizing the set of eigenvalues corresponding to a subset of the PCA vector basis. Benameur et al. [10] used a gradient descent optimization algorithm [24] to optimize a deformable model of the vertebrae. The optimization function was based on minimizing a logarithmic energy function between the projection of the candidate model and the image edges. In [18], deformation was done by Downhill Simplex optimization of the template model to fit projection lines. Baka et al. [12] optimized the energy function formulated between the image features and the 3D bone using conjugate gradients.

### 1.2.5 Overview

In previous attempts for bone reconstruction using x-rays, utilizing a statistical model was shown to be the widely accepted method. Currently, the major challenges to accurate reconstruction of bone models are the methods used to optimize the registration of the template (3 rotation + 3 translation parameters) in addition to the number of significant statistical modes of variation  $N_s$  (usually  $N_s > 30$ ). Pose optimization by itself could be successful in extracting the pose of a known 3D model as in [25],[26], but it would introduce

large pose errors for unknown shapes. As was mentioned in [27], the shape + pose parameter space is complex, with many local minima for the  $(N_s + 6)$  degrees of freedom. The optimization methods used in the literature are known to be of local nature. They are known to succeed in capturing the global minimum of a multi-model search space, only if they are initialized within the search space valley containing that minimum. This condition is not attainable in the current problem. A common solution to similar optimization problems is the use of stochastic optimization methods such as Simulated Annealing [26] or the Genetic Algorithm [28]. Such methods, by definition, require a very large number of iterations to converge, which would require an extensive amount of processing time. Furthermore, results are not guaranteed to achieve the global optimum.

In the literature, the number of radiographic images used for 3D model reconstruction is usually two. The challenge of using one image lies in the ambiguity of the bone template placement in space and its direct correlation to the model scale. In [29], the authors attempted to reconstruct four pelvises from a single AP image. They made the assumption that the distance between the pelvises and the imaging film was constant at 15 cm. Although such an OID is possible, the distance between the pelvis of a patient, standing or laying in the supine position, and the imaging table can vary significantly, which would introduce large magnification errors.

In this work, a new approach is proposed for 3D model reconstruction from two or more radiographs. Utilizing a statistical shape model, the registration problem is dealt with utilizing two calibration objects rigidly attached to the patient's femur and tibia. These targets capture

the relative bones' poses between images, which allow flexibility in the radiological setup in addition to normal patient motion between imaging sessions. After that, the exact bone poses are extracted using a novel pose estimation system that uses the bone's projected shape as an input. Given the correct registration, a statistical atlas is optimized in a novel deformation framework based on the Projection on Convex Sets (POCS) algorithm. This algorithm has the advantage of having a deterministic approach in reaching the best possible model that follows the statistical model and matching image features.

### 1.3 Contributions

This work is a collaborative effort from the research team of the Center of Musculoskeletal Research at the University of Tennessee, Knoxville. My contributions within this work can be outlined as follows:

- Developed a flexible, highly portable patient-specific bone model reconstruction method from x-ray radiography that utilizes current low-cost, low ionizing radiation traditional imaging and existing protocols.
- Developed a novel fast and accurate bone model reconstruction algorithm from two or more x-ray images based on statistical bone-specific shape models.
  - Incorporated POCS optimization that guarantees anatomical relevance of the reconstructed bones.
  - Incorporated a novel 2D/3D point registration methodology.
  - Developed an algorithm for automatic extraction and labeling of different anatomical 2D projections of bone regions.
  - Developed a robust, non-invasive 3D bone pose estimation system from radiographic imaging.

## 1.4 Organization

Chapter 2 provides a detailed explanation of the completed work in the different reconstruction modules.

- Section 2.1 describes the imaging options, requirements, and constraints.
- Section 2.2 explains the process of creating the statistical bone models used for patient-specific bone reconstruction.
- Section 2.3 lists the 2D x-ray image segmentation processes as a step to obtaining image contour features.
- Section 2.4 details the registration process of the template model within a simulated radiological scene, a prerequisite step to bone deformation, and how a calibration target is used to allow flexibility in the imaging requirements.
- Section 2.5 describes the novel bone deformation process and how it ultimately provides a patient-specific bone model.

Chapter 3 discusses verification studies performed on cadaveric and live patient cases to assess the accuracy of the bone reconstruction system and its feasibility to be used within surgical applications.

## Chapter 2: Materials and Methods

---

In this chapter, an overview of the imaging requirements for the bone reconstruction system will be discussed. Following that, the work completed within every module of the bone reconstruction system will be described separately with reference as to how the individual modules are integrated.

### 2.1. Imaging and Preprocessing

The system was designed for bone reconstruction from two or more images. Any imaging modality that produces digital radiographic output can be used, including Computed Radiography (CR), Digital Radiography (DR), Film Digitizers, or fluoroscopy. Exposure parameters should maximize image contrast, especially in joint areas. Radiographic scene properties, such as focal length and pixel spacing of the digitized image, are manually input to the system if not readily available in the image's file header.

Projections should be taken to maximize the amount of unique obtainable image information by minimizing mutual information between images. This can be done through scanning at maximized bone rotation difference between images. Using traditional protocols, the AP and the lateral (LAT) view are recommended. Image accuracy can be increased by adding extra image information through one or more oblique views. The bones can be imaged using long-film that captures the complete lower extremity within one image (Figure 7).



Figure 7 Example for a long-film case showing the AP view (left) and LAT view (right).

In the case that long-film is not available; short-film can be used to divide the lower extremity into three different sections (Figure 8):

- a) Proximal femur
- b) Knee
- c) Distal tibia





Figure 8 Example showing how the AP view was divided into three images

A calibration target was designed to be attached to the individual bones to capture the bone transformation between different images relative to the radiological scene for registration purposes. The design provides an ergonomic fit to the patient's leg contour. Semi-sphere slots were placed on the target's surface to provide a cavity where radio-opaque beads would be glued (Figure 9). Straps were allotted for tight fitting to the patient's leg (Figure 10).

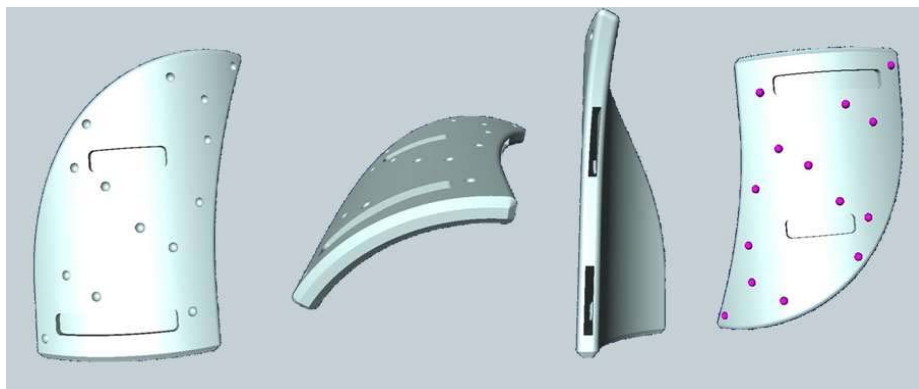


Figure 9 Calibration target.



Figure 10 Calibration target attached to leg.

The placement of the markers on the brace was chosen to cover as large an image area as possible in all the frames. A minimum of four beads needs to be visual in the image to allow accurate pose estimation. More beads were added to provide tolerance in case a subset of them was projected outside of the image field of view or were obscured by other high intensity objects.

Before any further processing, image data normalization is performed to standardize the data format and maximize image contrast, based on the current data greyscale dynamic range.

## 2.2. Bone Shape Modeling

Using a large dataset of bone models segmented from 3D CT scans, gender-specific statistical models are created for the bones of the knee joint. The statistical mean of these

models will provide the initial estimate of the patient's bone shape. The corresponding modes of variation, parameterized through a few number of variables, will be optimized within the morphing stage in order to fit the template bone shape to the set of extracted radiographic features. Figure 11 shows a summary of the complete statistical model reconstruction process.

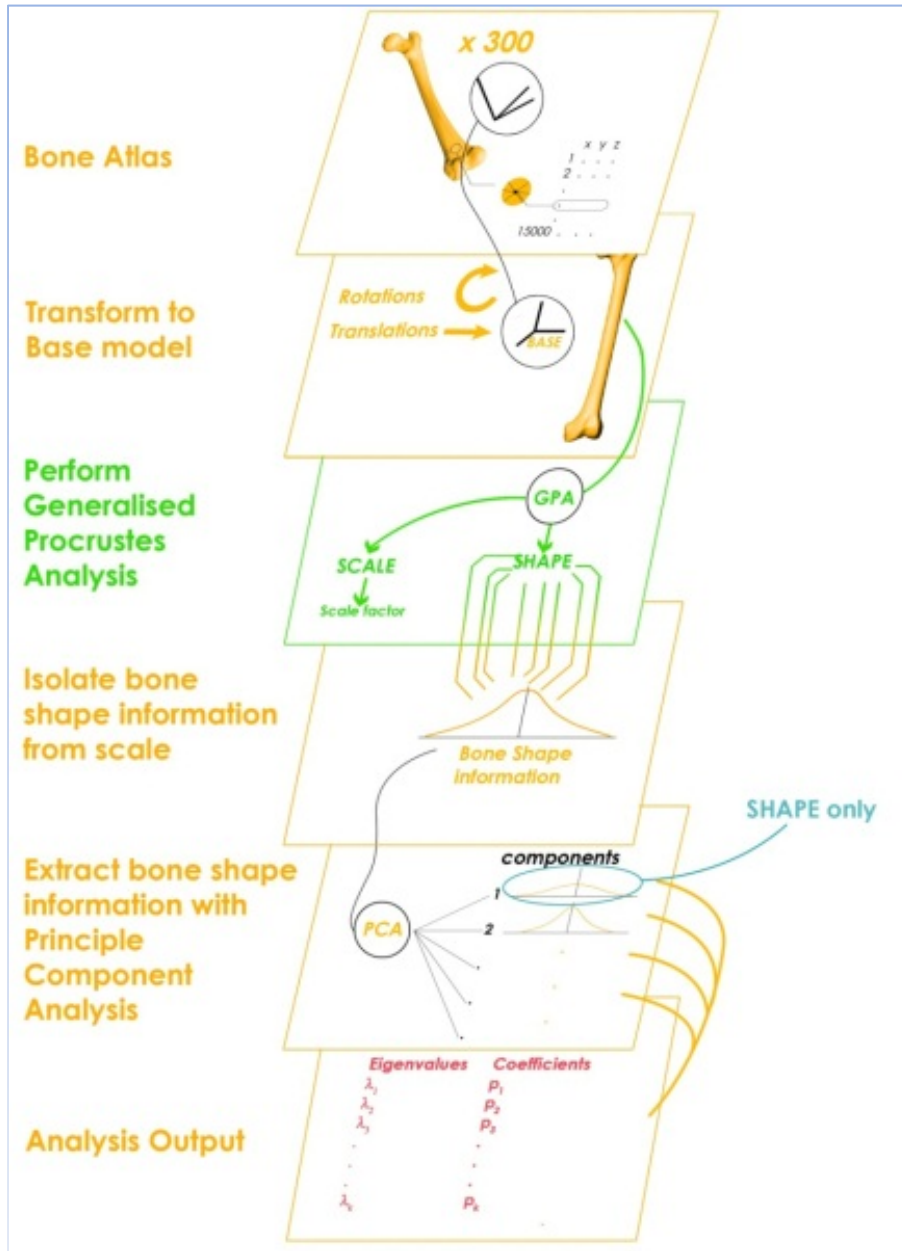


Figure 11 Statistical shape modelling process

### 2.2.1 Bone Model Dataset

The current atlas consists full femur and tibia bones obtained from the William M. Bass Donated Skeletal Collection from the University of Tennessee Anthropology Department, as well as life patient scans from clinical studies obtained by the Center of Musculoskeletal Research at the University of Tennessee. These bones were scanned using a GE Lightspeed 16 Slice CT scanner using 0.625 x 0.625 x 0.625 mm cubic voxels. The resultant DICOM datasets were loaded and manually segmented in Mercury Amira® or Avizo® to generate labels files. After that, high resolution triangulated meshes were created for every segmentation using the Computational Geometry Algorithms Library (CGAL). Due to the shape dissimilarity between male and female lower limb bones [30-32], a decision was made to sort the generated bone models by gender which would allow for the creation of gender-specific statistical models. Although the methodology is not specific to a certain ethnicity, due to availability the model dataset was restricted to samples of Caucasian descent. The number of bones used for each statistical model is shown in Table 2.

Table 2 Number of bones used to create the relevant gender-specific atlases.

Bone	Gender	Number of Bones
Femur	Male	200
Femur	Female	113
Tibia	Male	200
Tibia	Female	116

### 2.2.2 Template Bone

In order to normalize all the bones used to generate the statistical model, a template model is needed as a reference. The template bone should have sufficient vertices to accurately represent the expected bone detail, while minimizing the number of vertices to reduce storage and processing requirements. For that purpose, an adaptive curvature-based meshing with higher decimation in regions of interest was created.

In order to facilitate future steps, the template bone was also aligned with the z-axis, with the x-axis defined to be in the medial-lateral or lateral-medial direction (Figure 12). The template used was a right bone. All left dataset bones were mirrored before use for further processing, a widely accepted approach in dealing with laterality due to high similarity between right and left bones.

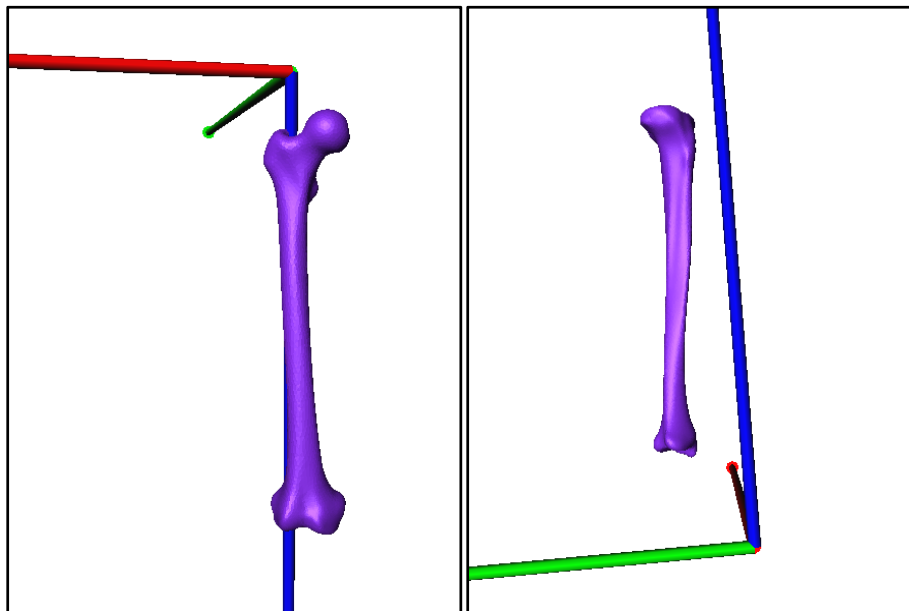


Figure 12 Template models.

### 2.2.3 Model Fitting

In model fitting, the template bone is affinely transformed in order to minimize its distance to the high resolution bone model. The transformation is calculated in an inverse manner (aligning the high resolution model to the template model and then using the inverse matrix to transform the template model). The fitting steps are as follows:

1. Principle axes alignment.
2. Scaling using bounding box z-ratio.
3. Centroids alignment (Figure 13).
4. Multiple ICP alignment initialized scanning (Figure 14) to avoid local minima.

Initialization was done to follow combinations of:

- a) 0 and 180 degrees x-rotation.
  - b) 0 and 180 degrees y-rotation.
  - c) 0, 90, 180 and 270 degrees z-rotation.
5. The ICP alignment resulting in the least RMS surface error is used.

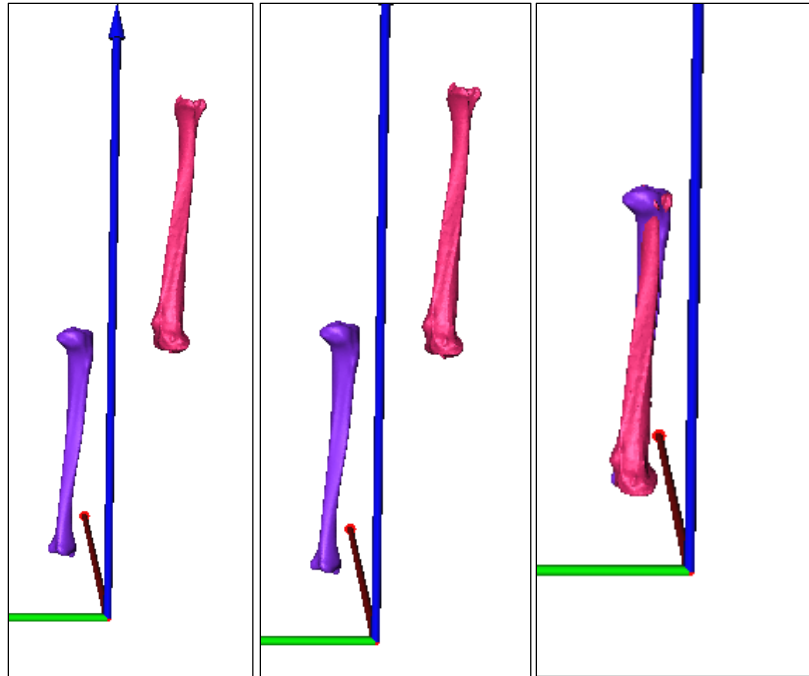


Figure 13 Image showing fitting steps between template model (purple) and high resolution model (pink). From left to right: principle axis alignment, scaling, and centroid alignment.

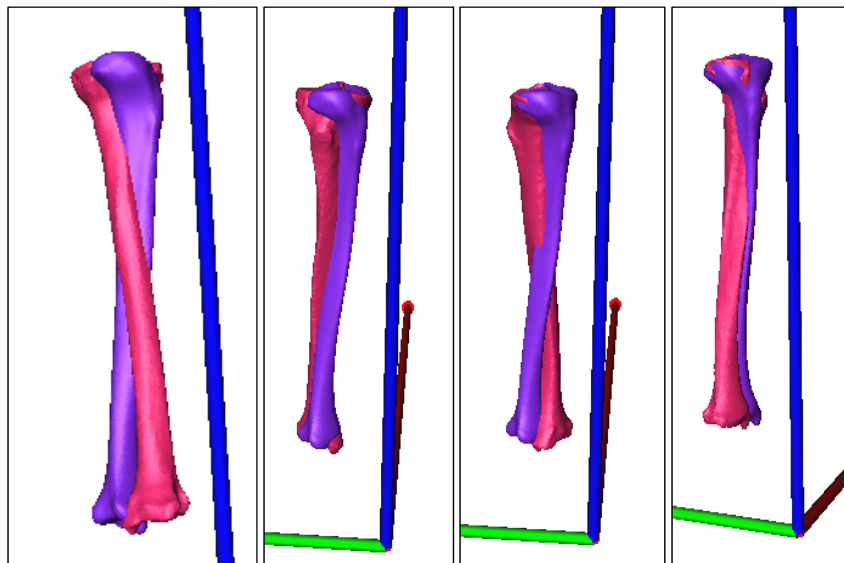


Figure 14 Image showing different pose initializations between template model (purple) and high resolution model (pink).

Figure 15 shows an example distance map between the template and the dataset model after the model fitting step.

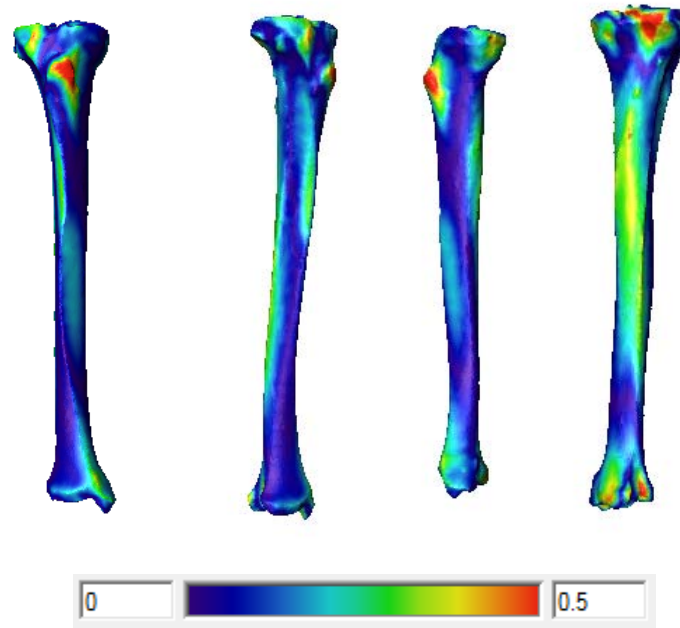


Figure 15 Images showing a distance map between the template and high resolution model after ICP alignment in mm.

#### 2.2.4 Template Warping and Correspondence Matching

Mutual Correspondence Warping (MCW) (Figure 16) is used to warp the template bone mesh to the generated meshes. Basically, point correspondences are picked in both directions and, in an iterative manner, the closest vertex-to-vertex correspondences are found from the template to the new model; but, correspondences are also found from the new model to the template model. Using both of these point correspondences, points on the template mesh are moved toward locations on the new mesh using a non-symmetric weighting of the vectors of correspondence. More information can be found in [31].



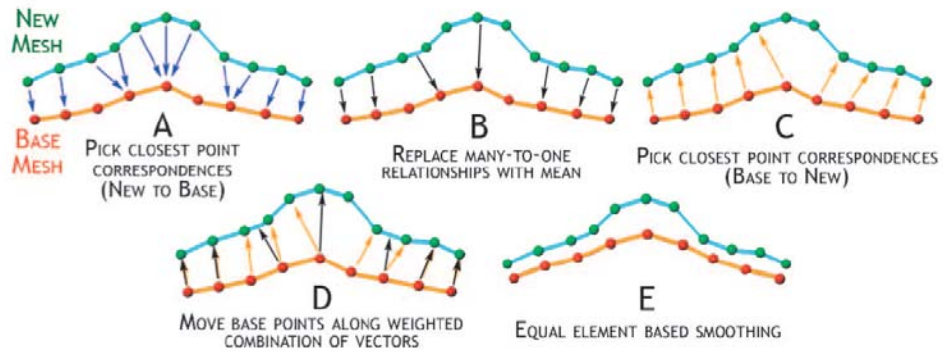


Figure 1. Two dimensional example of the MCW algorithm. The two meshes prior to algorithm are initially separated. The closest point correspondences from new mesh (dark/red) to base mesh (light/green) are calculated (A) and many-to-one relationships are replaced with mean vectors (B). Closest point correspondences from base mesh to new mesh are found (C) and a linear combination of vectors defined in steps B and C is used in (D) to warp the base mesh which undergoes an equal element smoothing (E). This process is performed iteratively until the relative error between iterations no longer changes.

Figure 16 Mutual correspondence warping. Copied from [31].

Figure 17 shows the distance map between the template and the dataset model after the model fitting step.

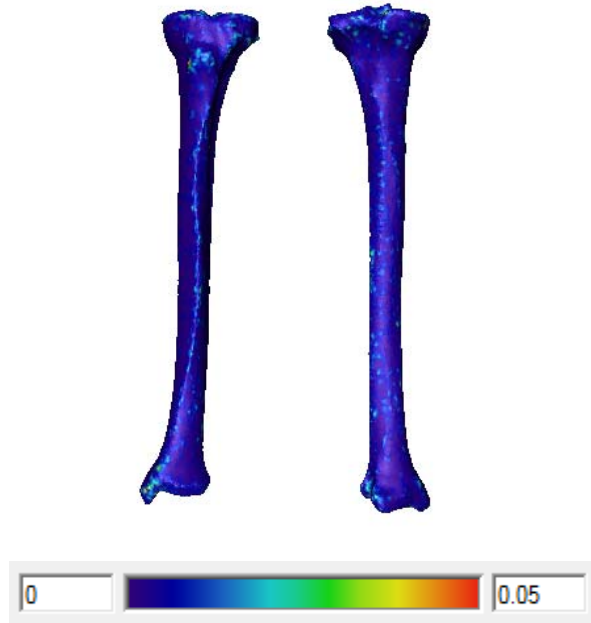


Figure 17 Images showing a distance map between the template and high resolution model after template warping in mm.

### 2.2.5 Partial Bone Generation and Alignment

In order to allow reconstruction from short-film x-rays, a partial bone statistical model would be needed. Since the template bone is aligned to the z-axis, z-level thresholding (Figure 18), in a bounding box sense, is used to crop the bone part of interest. This gives a set of vertex indices that will be extracted from all the atlas bones to give correspondence-matching partial atlas bones. For the current atlases, partial bones were extracted at the 20% z-level. Post processing is done on the cutting end of the bone to project the edge vertices of the cutting plane, smoothing the open end. This is necessary to eliminate the jagged edges expected due to triangulation resolution limitations.

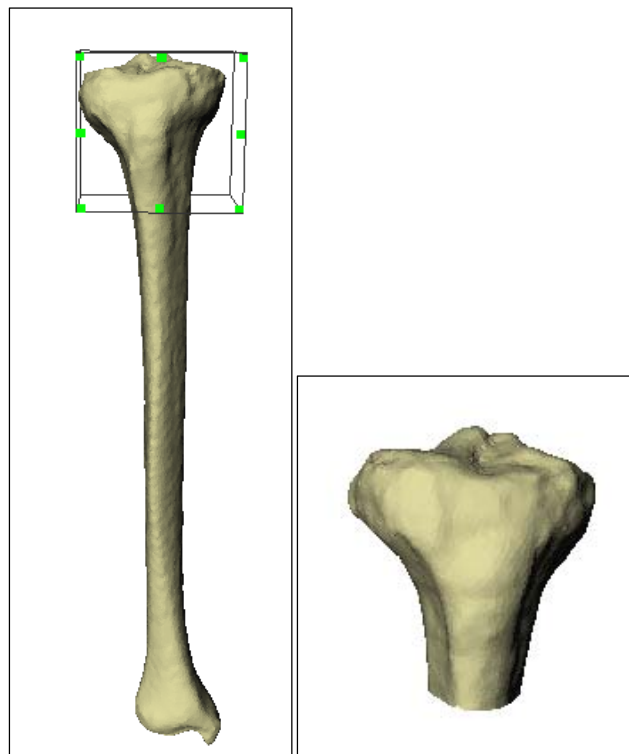


Figure 18 Partial bone extraction.

The resultant partial bones are then aligned in space. This is done in three passes:

1. Center template partial bone around the origin.
2. Rotate the template bone so that it is aligned to follow the following specifications:
  - a) The z-axis is in the distal-proximal direction.
  - b) The y-axis is in the posterior-anterior direction.
  - c) The x-axis is in the medial-lateral direction.
3. Align all partial bones to the transformed template bone using vertex correspondences [33].

### 2.2.6 Decoupling of Scale from the Statistical Shape Model

The bones generated so far are adequate for atlas generation. Nevertheless, in order to allow for more concise representation of shape, scale needs to be factored away from the shape representation. This is done by an extra scale normalizing step which uses Procrustes analysis:

1. Calculate the mean of the set of partial bones.
2. Normalize the scale of all bones to have the same scale of the mean bone. The scale metric used was the Frobenius norm.

$$S(x) = \sqrt{\sum_{i=1}^n [(x_i - \bar{x})^2 + (y_i - \bar{y})^2]}$$

3. Align all scaled bones to the mean model using point correspondence matching [33].

### 2.2.7 Atlas Generation

A mathematical representation of an  $n$ -point shape in  $k$  dimensions is used to concatenate each dimension into a  $kn$ -vector. PCA is performed on the correspondence-matching, scale-normalized bone models as in [13].

### 2.3. Feature Extraction

Image features represent the ground-truth silhouette projection the template model deformation aims to achieve. On the 3D bone, it can be shown that the strongest internal edges on the x-ray images appear in areas where the 3D bone surface normal is parallel to the image plane. Other bone regions would show as textural information that cannot be utilized within a surface reconstruction framework. Figure 19 and Figure 20 show a 3D-rendered distal femur and proximal tibia at different poses to highlight example bone areas that are expected to produce clear edges on the x-ray images.

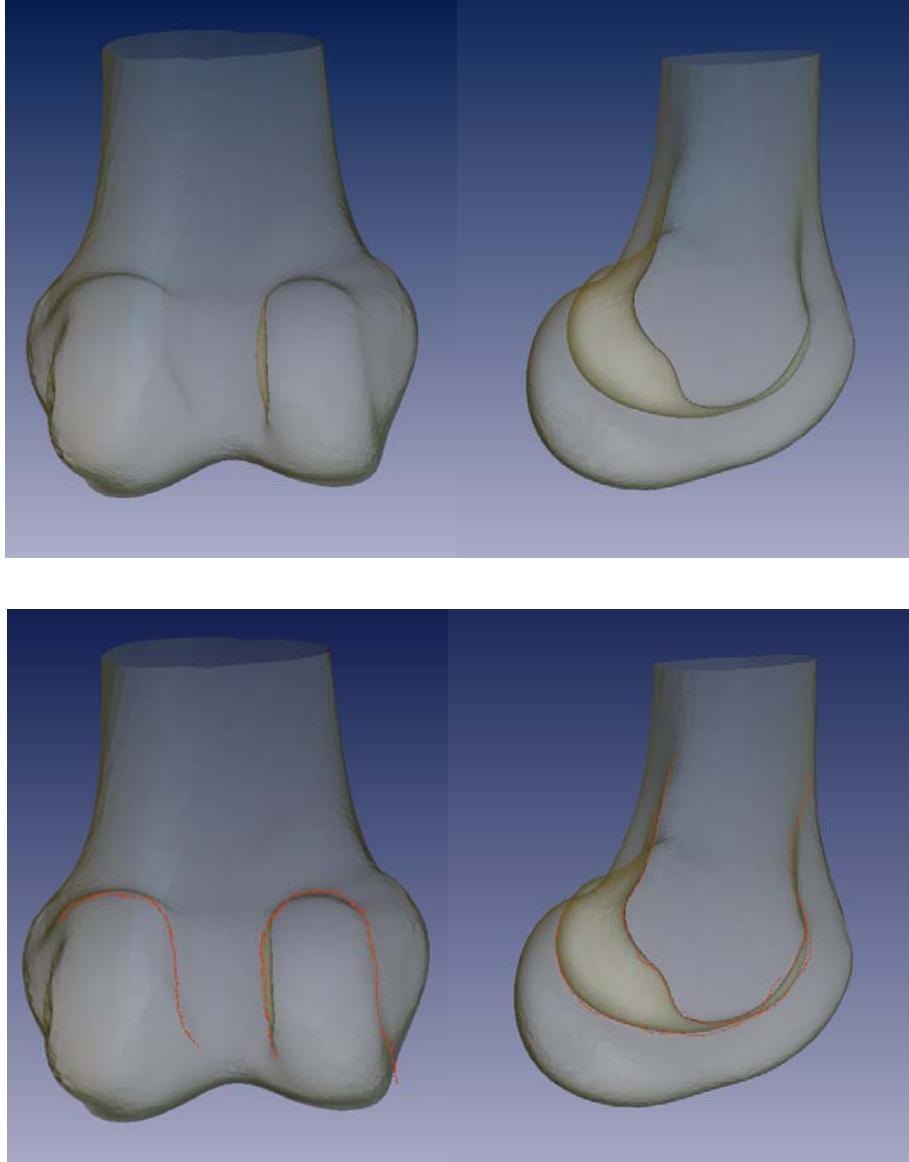


Figure 19 Template distal femur shown in transparency mode (top) and candidate contour features highlighted in red (bottom).

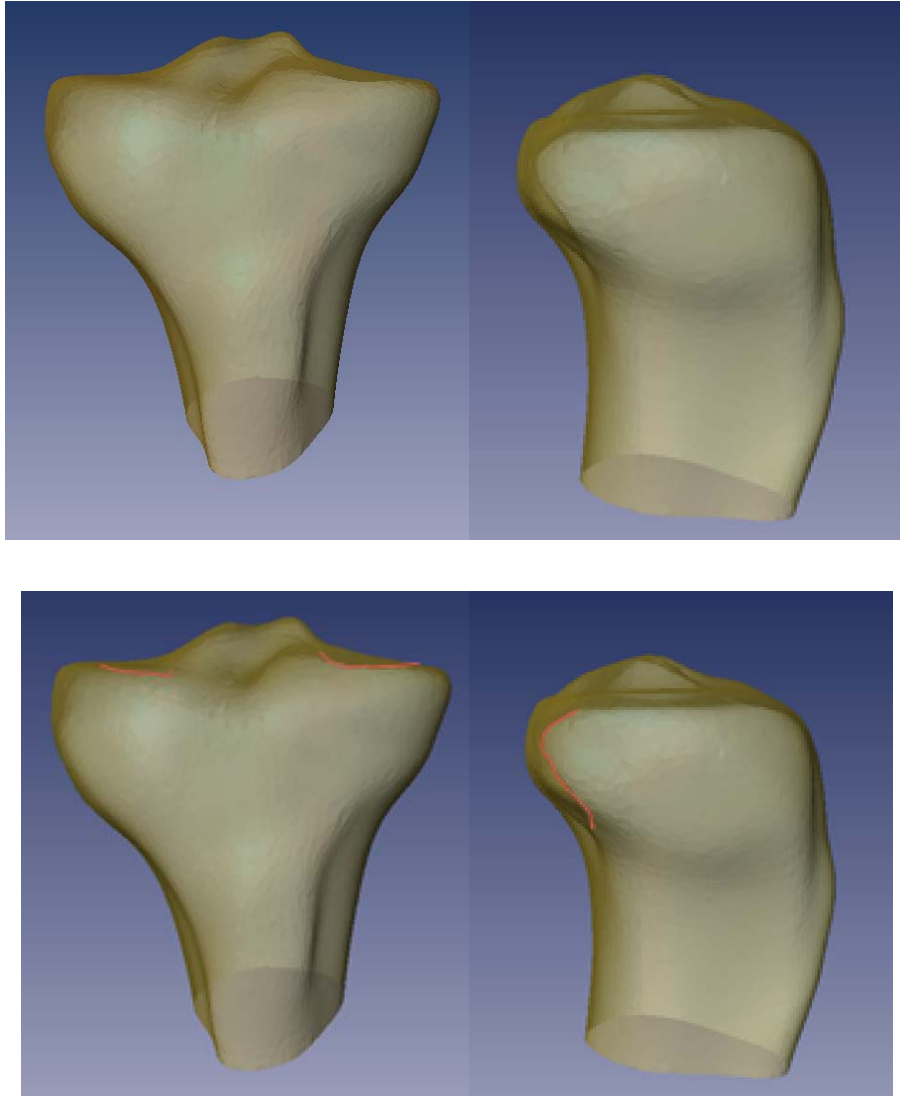


Figure 20 Template proximal tibia shown in transparency mode (top) and candidate contour features highlighted in red (bottom).

Figure 21 and Figure 22 show how the candidate internal contour features appear on two radiographic cases.

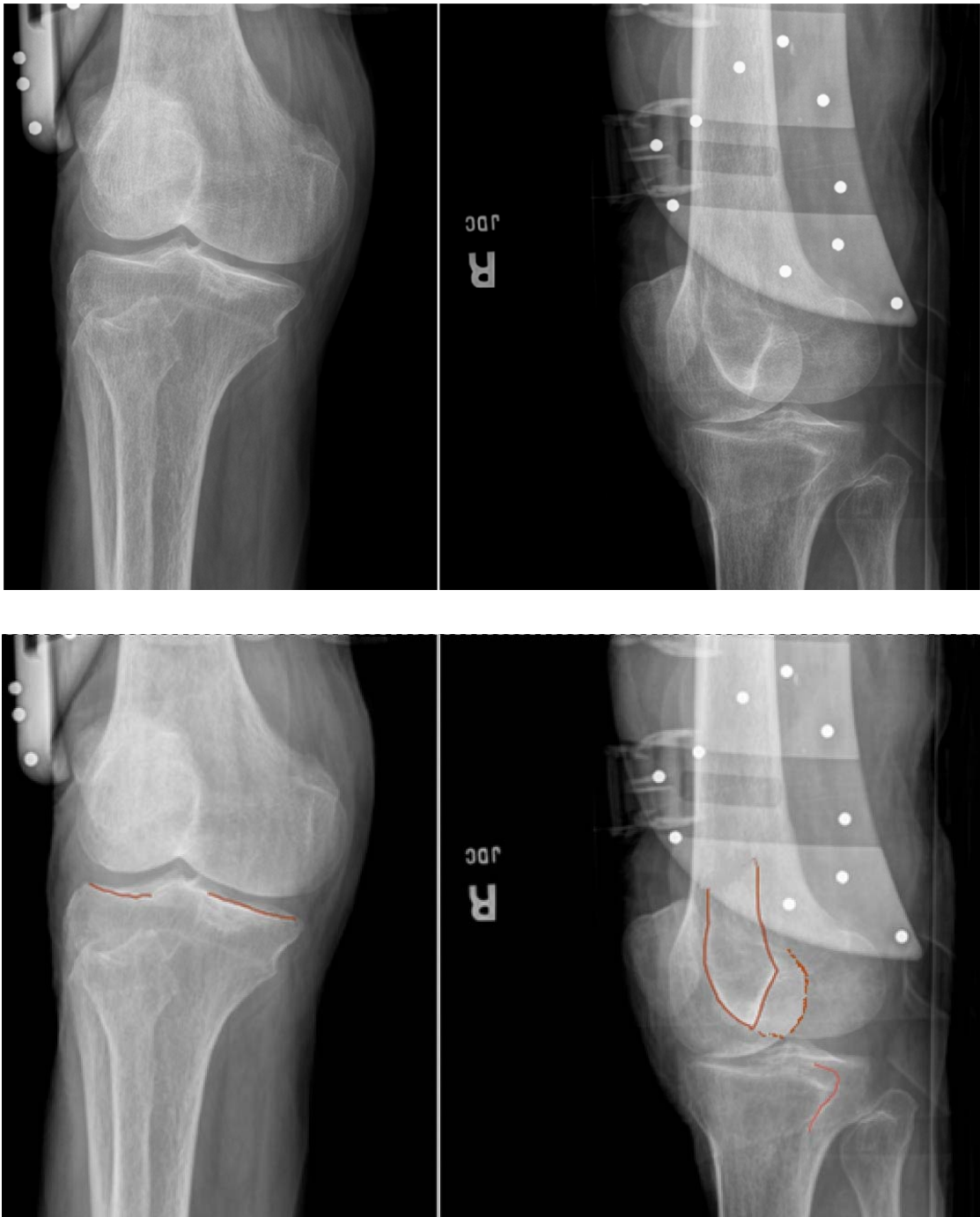


Figure 21 Case 1. Original images (top) and candidate internal contours highlighted in red (bottom).

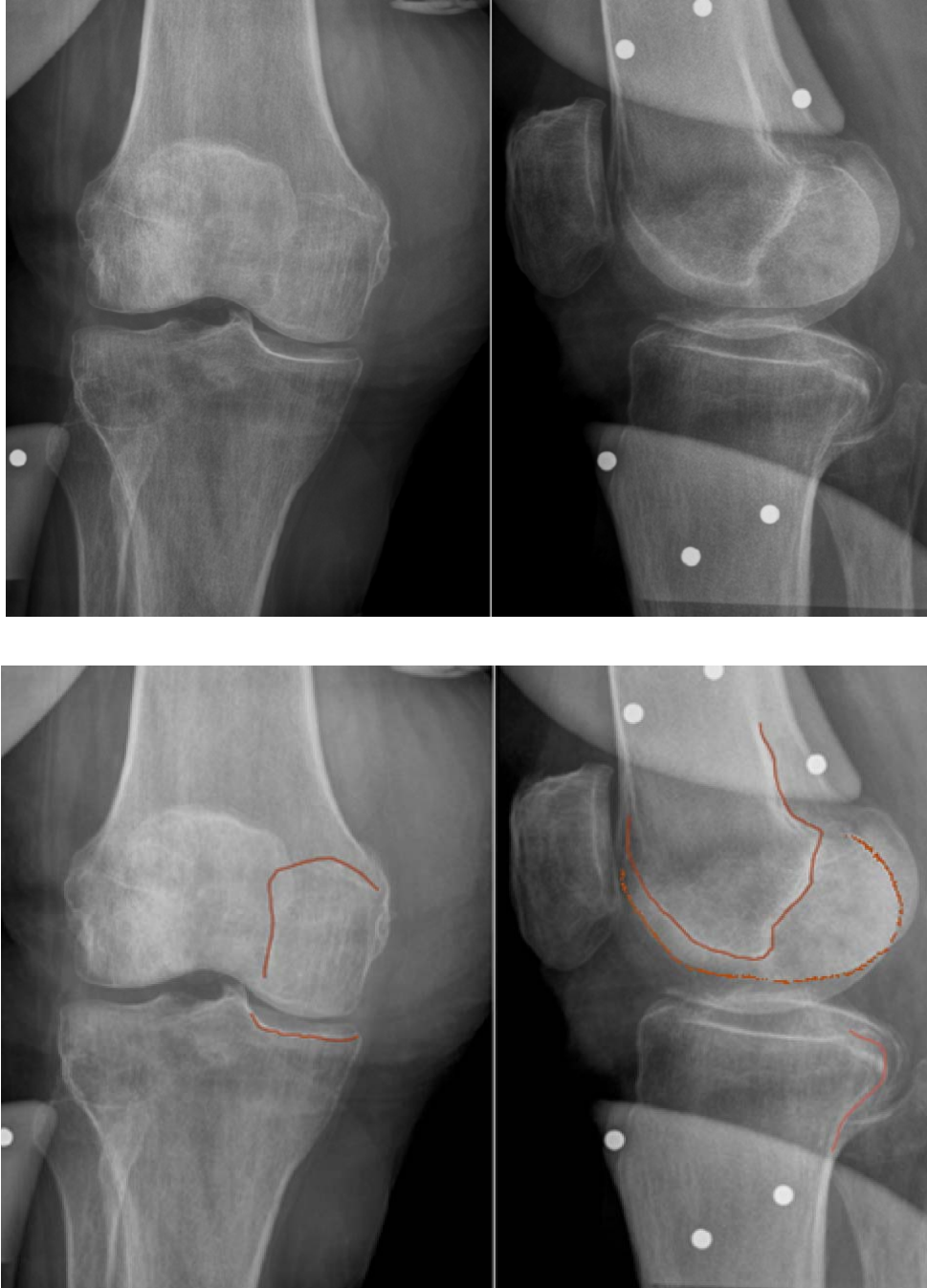


Figure 22 Case 2. Original images (top) and candidate internal contours highlighted in red (bottom).

In this work, bone contour features were extracted manually and automatically. Both methods are described in the following sections.



### 2.3.1. Manual Segmentation

A manual method remains to be the gold standard for segmentation. In this technique, the user selects points outlining the outer bone contour (Figure 23). After that, individual internal contours are individually defined (Figure 24). Although robust, the manual segmentation process remains to be a tedious and challenging task, especially within areas of lower contrast like the knee gap and patella-femoral joint in the lateral view [11].

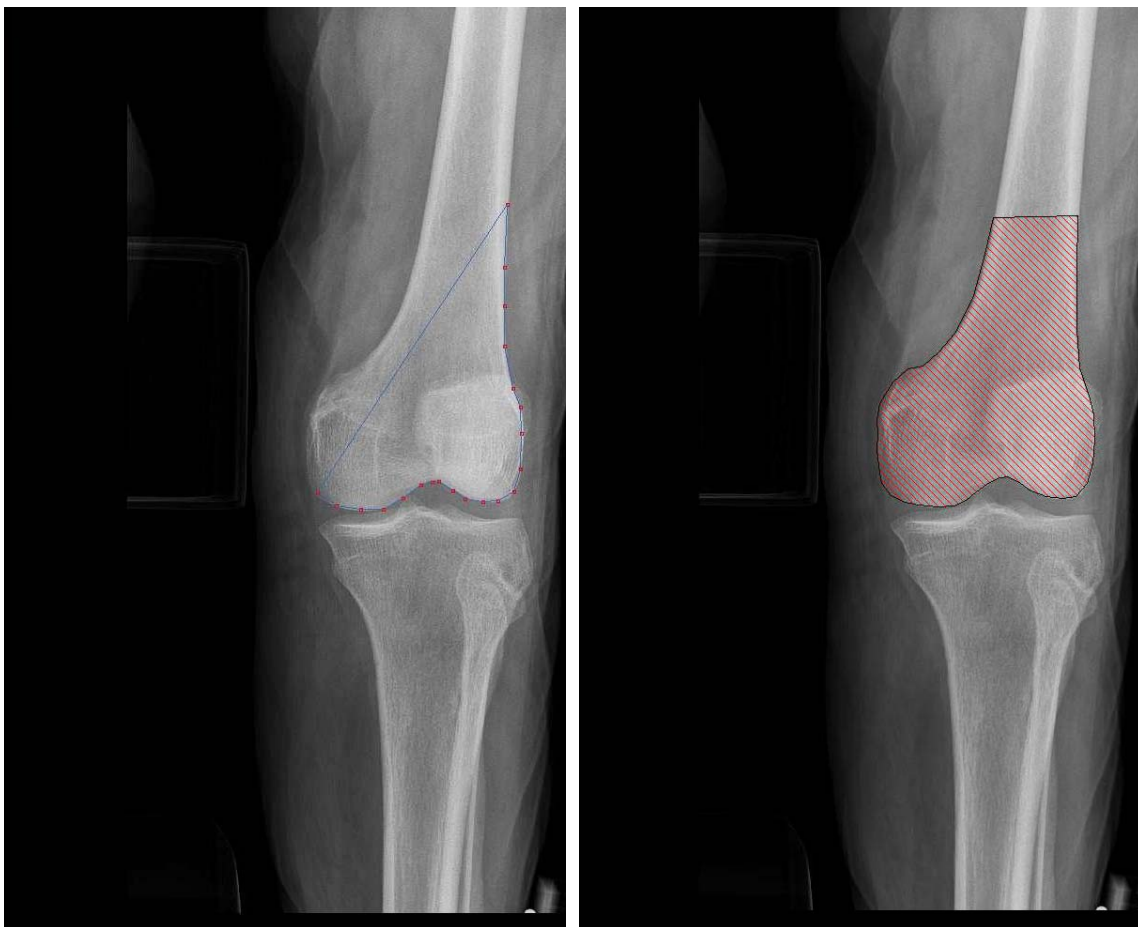


Figure 23: Manual image segmentation (left) and segmented image (right).

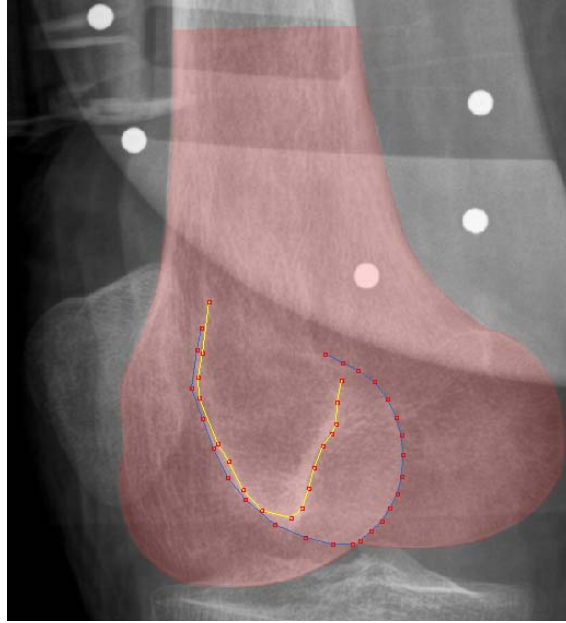


Figure 24 Image showing the segmented outer contour shaded in red with the internal contours manually selected.

### 2.3.2. Automatic Segmentation

Automatic segmentation was built to accelerate the contour segmentation process and provide accurate estimates at areas where the contour is not clear. Using a method similar to [13], a statistical atlas of bone contours was generated using synthetic projections of our database of 3D bones. A template average bone contour from the statistical atlas is semi-automatically registered and scaled to the bone's image. Contour deformation is then automatically performed to fit the target bone image based on the image's intensity gradients.

#### 2.3.2.1 Atlas Creation

Figure 25 shows a flowchart highlighting the 2D contour atlas generation process.

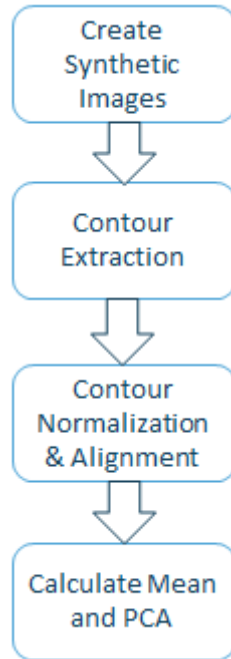


Figure 25 2D contour atlas creation flowchart.

Synthetic images were created using a database of 3D bones. Every bone was placed in a simulation graphics scene and off-screen renderings were taken at all expected x-ray bone poses. Figure 26 shows samples for the synthetic images created.



Figure 26 Image showing synthetic image samples.

The bone contours were then automatically extracted to generate the contour database for the statistical contour atlas. In order to generate the atlas, the contours were normalized, aligned, and point correspondence was obtained. Using the bone correspondences, PCA [34] was performed to obtain the mean and modes of variation of the contours.

### ***2.3.2.2 Mean Contour Initialization***

Figure 27 shows how the user interactively registers the template bone contour to the x-ray image to initialize the segmentation process.



**Figure 27** Initialized bone contour.

### ***2.3.2.3 Contour Fitting***

Figure 28 shows the contour fitting process. Given an initialized template contour, every point on the contour is moved in its normal direction towards the pixel representing the strongest edge. That pixel is detected by applying Savitzky-Golay [35] smoothing on the

intensity profile of the template point. The point having the maximum absolute gradient on the smoothed profile would represent the target pixel  $P_{max}$  (Figure 29).

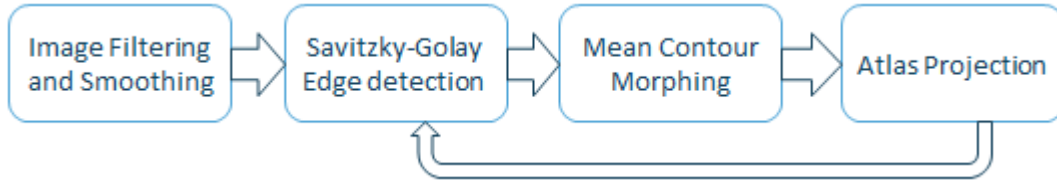


Figure 28 Contour fitting flowchart.

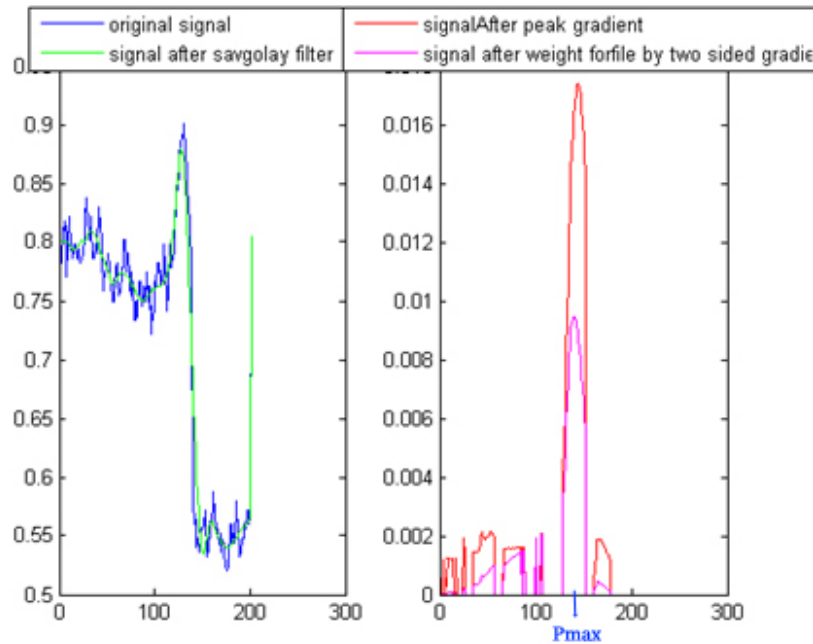


Figure 29 Edge detection. Profile signal (left) and profile gradient (right) showing the detected profile edge point index,  $P_{max}$ .

After moving all the contour points towards the closest edge point, the contour is projected onto the contour atlas basis vectors to constrain the morphed contour to comply with the statistical modes of variation. This also insures that falsely detected edges do not

distort the final segmentation. The process is iterated until the relative RMS change in the contour shape falls under a pre-specified threshold. Figure 30 shows the segmentation process for a single fitting iteration. Figure 31 shows the final segmentation.

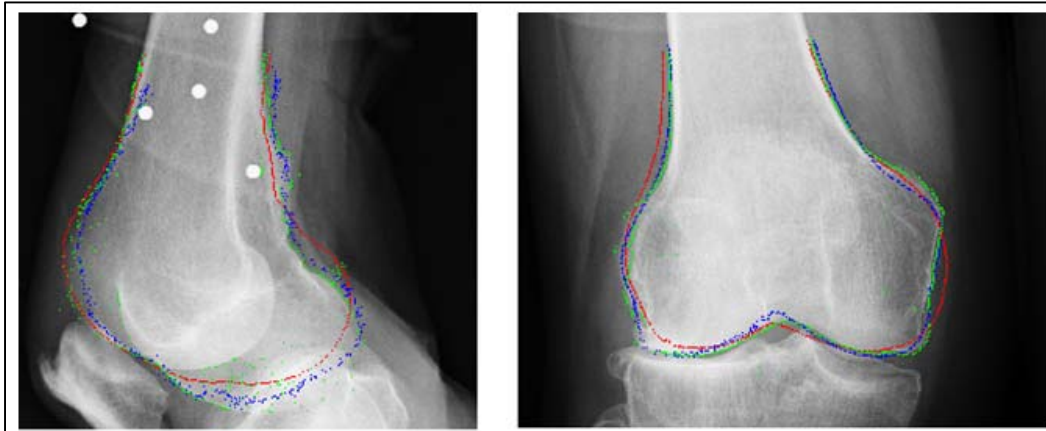


Figure 30 Image showing the fitting progress. The red contour represents the initial registered contour. Green points are edge points detected using the Savitzky-Golay filter. Blue points represent the contour after projecting back to the atlas.



Figure 31 Final segmentation results.

## 2.4 Registration

The registration module aims to extract an accurate estimation of the pose parameters ( $T_x, T_y, T_z, R_x, R_y, R_z$ ) of the bone within the radiographic scene. An object's pose, is the transformation needed to map the object's model from its inherit coordinate system into agreement with the sensory data [36]. Given a 3D template model within its own object coordinate system and the calibration target's relative pose used to capture the object's transformation between images, it is required to estimate the object's pose at which the individual images were captured. Given the correct pose, a simulated radiological scene will be built for every image, where the x-ray source, image plane, and the bone template would be placed in a relative manner similar to that of the original radiological arrangement. This would provide the required setup for bone morphing.

The distance at which the template is placed relative to the image plane directly impacts the scale of the reconstructed bone due to the perspective projective nature of radiography.

Figure 32 shows a simulated radiological scene. For a given SID, the PMF can be calculated as follows:

$$PMF = \frac{SID}{SID - OID}$$

where OID is the Object-to-Image distance.

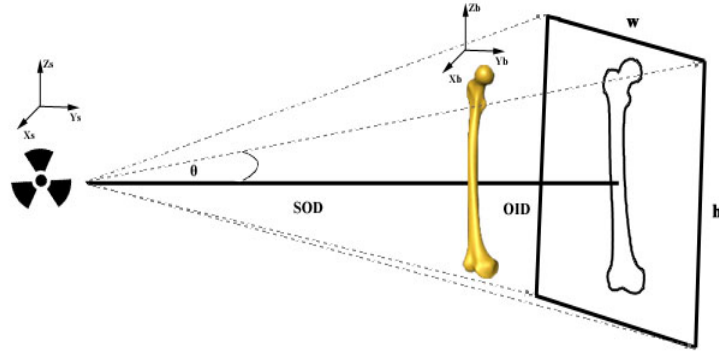


Figure 32 Projection model of the radiographic scene.

Figure 33 shows how the PMF is affected by the SID and OID.

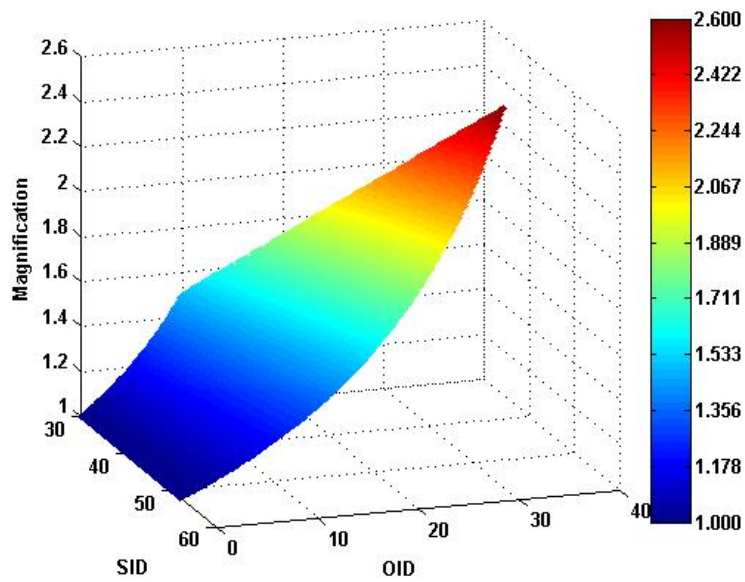


Figure 33 Plot showing magnification trend as SID and OID change.

Figure 34 shows that, given a constant SID for every 1 cm of OID error, there is 1-2% magnification error for the bone. Such an error would directly render a reconstruction unsuitable for applications requiring high accuracy, such as implant sizing.



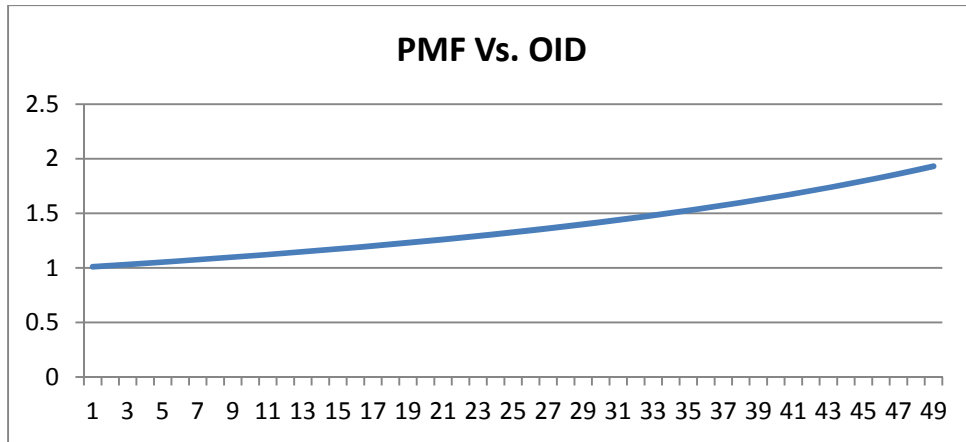


Figure 34 PMF vs. object-to-image distance for a constant SID.

In the following sections, it will be illustrated how the exact pose is estimated individually for two or more pose-independent images.

### 2.4.1 Radiological Scene Simulation

The science of visual perception has extensively studied the physical properties of imaging since the invention of the first pin-hole camera in the 10<sup>th</sup> century by Alhazen. This knowledgebase has been packaged in computerized visual simulation libraries [37, 38] that model the optical and physical models, with the goal of building realistic graphical simulations. Furthermore, these libraries have been integrated into hardware Graphical Processing Units (GPUs) for rendering speed and systems integration [39, 40]. This work takes advantage of such advancements in the bone reconstruction process. The perspective nature of x-ray radiography allows the use of the pin-hole camera model for x-ray imaging simulation. Table 3 shows an analogy between radiological setups and perspective imaging. The result is a simulation framework that provides systematic, hardware-accelerated template model evaluation, comparison, and morphing.

Table 3 Analogy between x-ray radiography and perspective imaging.

Radiology	Perspective Imaging
X-Ray Source	Pinhole
Film/Sensor	Image
Patient's Bone	Object
Source-to-Image Distance(SID)	Focal Length
Object-to-Image Distance (OID)	Object Distance

For every image of the radiographic dataset, a graphics simulation of the radiographic scene (like the one shown in Figure 32) is built. The x-ray source is represented by a perspective camera model simulating radiological beam divergence. Within that camera's field of view, a template bone model is placed at a relative pose similar to that of the actual bone's pose within the radiological scene. Image rendering takes place on an image of the same size of the x-ray image, placed at a distance equal to the SID to the camera. The world coordinate system was defined to be at the center of the image plane.

Since no limitations are enforced on technicians moving the x-ray source-to-film distance, it is assumed that there is an unknown SID for every radiograph. Given that this value is critical for building the radiographic scene simulation, the software attempts to read this value from the image file header if the image is in the DICOM format. Otherwise, the technician can manually input the focal length, as read on the x-ray source control unit, or measure by tape. The value could also be extracted automatically by a simple calibration target, as explained in [41].

For every dataset image of width  $W$ , height  $H$ , and pixel dimensions  $(S_x, S_y)$ , given the input SID, the simulated scene is built as follows:

- The camera is assumed to be a point source and is placed at  $C_{loc} = (0, -SID, 0)$ .
- The image plane is placed at the  $Y = 0$  plane, with the top-left corner placed at  $(-u_0, 0, v_0)$  and the bottom-right corner placed at  $(u_0, 0, -v_0)$  where

$$u_0 = \frac{WS_x}{2} \quad v_0 = \frac{HS_y}{2}$$

- The template model will be placed within the cone defined between the camera and the corners of the image. The exact pose will be extracted in the next sections.

#### 2.4.2 Calibration Target Pose Extraction

Given an x-ray image showing four or more calibration target beads (Figure 35), the goal of this module is to extract the pose of the calibration target in the world coordinate system.

This is done in three steps:

1. Bead image extraction.
2. Initialization and establishing 2D/3D correspondences.
3. Pose optimization.

The complete process is repeated for all images in the dataset.



Figure 35 Radiograph of the leg with the calibration target attached.

#### ***2.4.2.2. Bead Extraction***

Bead extraction aims to extract the centroid of each bead image projection. This is done by thresholding the image at various levels, then using morphological operators to remove any objects that contain lines longer than the bead diameter (Figure 36). The morphological masks are defined based on the expected size of the beads in pixels. This is calculated, assuming no projection magnification exists, and dividing the physical 3D bead radius (2.25 mm in the current brace) by the image pixel size. This assumption would lead to a size that is smaller than the actual projection disc size, because the PMF is always greater than unity. Since the OID is not known yet, this is the more practical approach, to ensure that all the beads are detected successfully, and not eliminated by the disc morphological operators.

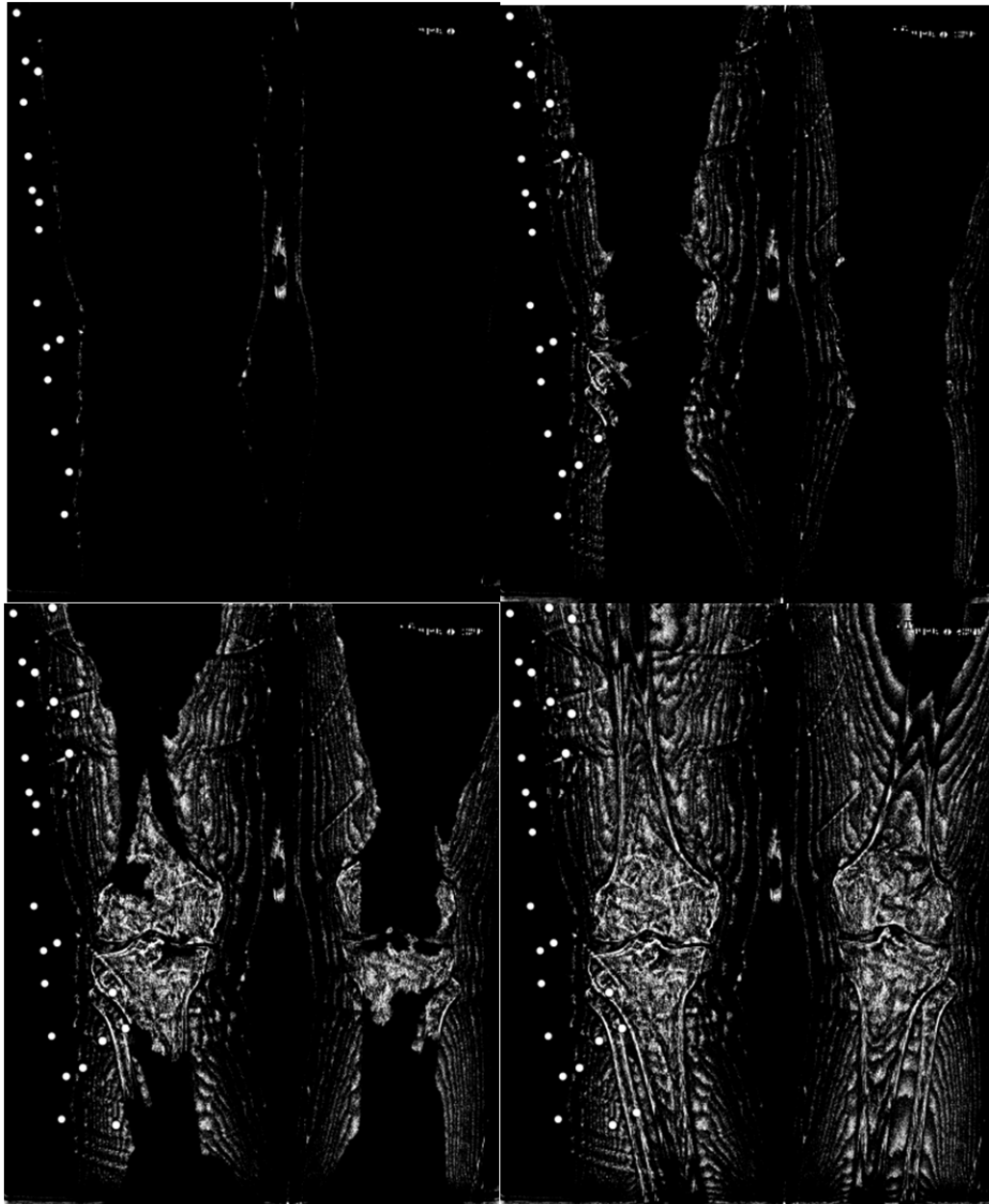


Figure 36 Multilevel Thresholding applied on x-ray image to extract beads.

Figure 37 shows the final extracted beads. Every bead is then isolated and labeled, and the center of each bead is calculated as the mean of the object's connected region.

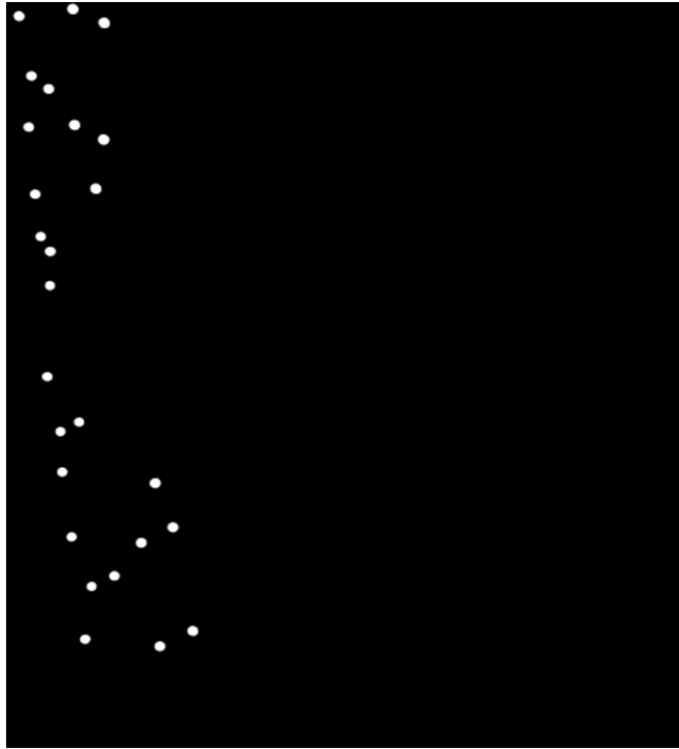


Figure 37 Extracted Beads

### *2.4.2.3. Bead correspondence*

In order to extract the pose of the calibration target, the extracted beads need to be identified, and the corresponding bead on the calibration target needs to be known. The latter is done semi-automatically using an interactive manipulation tool as shown in Figure 38. The manipulator tool contains a model of the target that the user can translate and rotate, then visualize the resultant bead projection. The user would manipulate the target, until each bead

projection closest to its corresponding x-ray bead image. This tool takes advantage of the simulated radiographic scene, and undergoes perspective projection for a brace model onto the x-ray image to give visual feedback.

Once the user is done with the initial registration, he initiates the automatic pose optimization step.

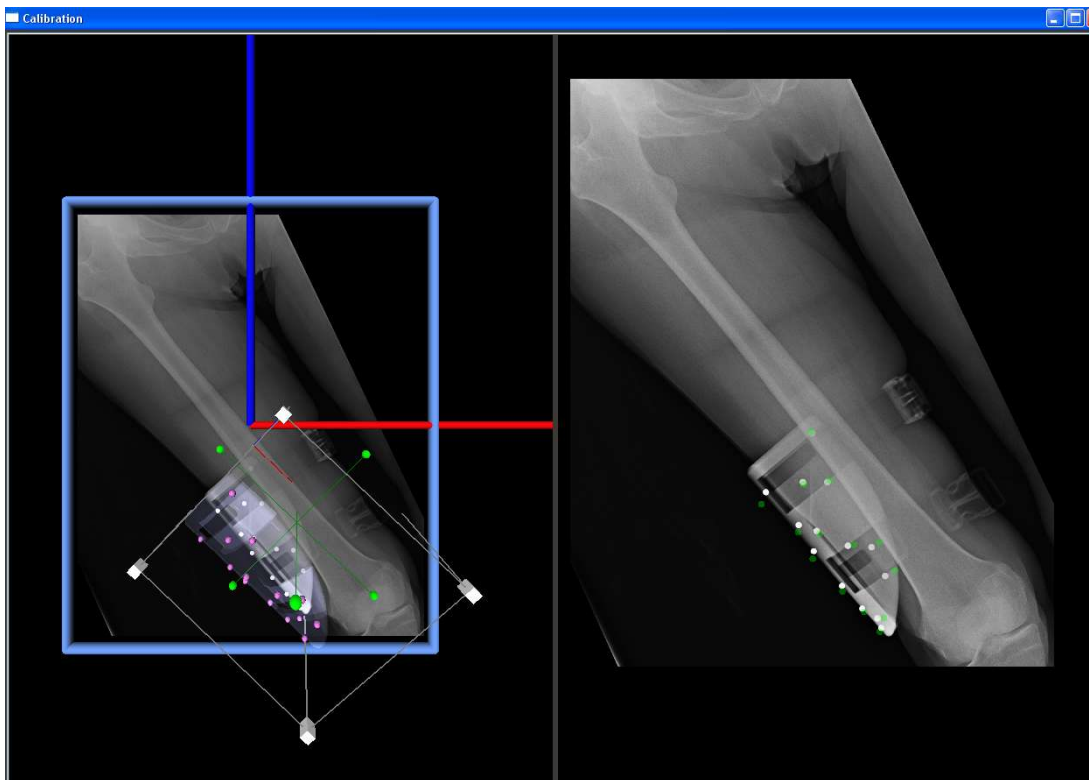


Figure 38 Semi-automatic brace initial placement to establish bead correspondences

#### *2.4.2.4. Calibration Target Pose computation*

Given the 3D brace bead locations in 3D and their corresponding extracted bead centers, pose of the brace ( $T_x, T_y, T_z, R_x, R_y, R_z$ ) is optimized, so that the bead projections would perfectly match the x-ray bead images.

The pose was optimized using Powell's direction set method [42] to minimize the sum of the Euclidean distances between the bead projection centers and the detected x-ray bead image centers. This optimization method was used because it doesn't need the calculation of the complex derivatives of the mathematical formulation of the fitting problem.

Powell's method can be summarized as follows:

A set of initial search direction 6-D vectors (corresponding to the 6 pose variables that need to be optimized) are created. For every direction, a bi-directional search along each search vector is performed. After saving the best score, and its corresponding pose, the direction responsible for it is deleted from the direction set to eliminate its influence upon further iterations. New directions are then created by combining existing directions. Iteration is done until no improvement is noticed.

Powell's method is still considered to be a local optimization method. To insure the global minimum is captured, a Monte Carlo sampling of the initialization pose is done. A Gaussian distribution was used, with a mean centered at the manually initialized pose. The sampling distribution variance was defined individually for the pose parameters giving higher



variance to  $T_y$  (10 cm) than  $T_x$  and  $T_z$  (2 cm), to make sure depth is captured. Variances for  $R_x$ ,  $R_y$ ,  $R_z$  were initialized using the same value (5 degrees). The variance values were empirically defined.

### 2.4.3. Model Rotational Pose Estimation

3D pose estimation of a bone model from a 2D image is a well-established problem in the field of computer vision. POSIT [43]: Given at least four non-coplanar 3D points and their corresponding 2D projections in the image, and the focal length of the camera, the algorithm is able to estimate the object's pose. This is done by first assuming orthographic projection, then solving a set of linear equations for initial pose estimation. After that, iterations are done, to solve for correct for perspective scale and pose optimization.

Another common method is RANSAC[44], which is commonly used in situations when there is a large number of image feature points and no correspondences. At least 3 points of the 3D model are selected, and then 3 random samples are selected from the image feature points. Given these hypothesized correspondences, the model pose that best fits the 2D features is computed. After that, the rest of the model is projected to the image, and number of feature matches (consensus set) is calculated. After  $N$  trials, the pose with the largest number of matches is the final pose estimation. This method has the advantage of being robust to feature outliers, but can be problematic due to the large number of possible match combinations ( $N^3 * M^3$  where  $N$  and  $M$  are the number of 2D and 3D landmarks).

As described, in order to use the previous pose estimation methods, correspondences between model points and their related 2D projections are required. Such a prerequisite is not attainable in the present problem because;

- a) The 3D model representation of the imaged bone is not available, since it is the final target of the system.
- b) The smoothness of bone anatomy and the projective nature of radiography make the accurate detection of 3D landmarks and their corresponding projections a challenging task.

A different approach has been taken for pose estimation. Taking into account the fact that the projection shape of the bone varies considerably with rotation, the problem of pose estimation is dealt with as a shape retrieval problem.

#### ***2.4.3.1 Feature Extraction***

This module is responsible for the extraction of contour shape features from the segmented bone contours. These features would collectively uniquely identify the contour shape, and hence, the bone 3D rotation that created such a pose. A detailed explanation of the method of feature extraction process will follow.

##### **2.4.3.1.1. Contour Normalization**

A contour shape representation can vary, depending on its position, size and orientation, or on the choice of starting point. The goal of this preprocessing step is to standardize the contour input to subsequent stages. The normalization is done through the following steps;

### *Starting point Normalization*

For any phase-dependent contour processing method, changing the starting point would result in a phase shift that could affect the extracted features' values. The normalizing of the starting point of contour traversal would eliminate such effect, facilitating the processes of contour region classification, and pose learning.

For partial bones, the cylindrical shape of the bone shaft provides a convenient trimming region, where the contour traversal could start, without losing important contour features. The trimming would result in discontinuity in the contour at the cut-off level. The two points at that discontinuity would represent the starting and ending point of the contour. Choosing the traversal direction (clockwise or counter clockwise) would indicate the starting point, as the point which when initially traversing from, results in no discontinuity until the end point is reached.

As for continuous contours, the starting point is selected according to the bone's specific features in a manner that provides consistency. For the femur, that point was selected as the top of the femoral head region. As for the tibia, it was chosen to be the tip point of the tibial malleolus.

### *Number of points normalization*

X-Ray bone contours can have a wide range of number of points. This could be due to the difference the size of the imaged bones, the image pixel resolution, and/or the radiological imaging parameters. The segmentation of these bone projections would consequently have an inconsistent number of contour points, resulting in unneeded complications in further

processing steps. Moreover, the large number of the original contour points would require much higher processing and storage requirements than what is theoretically needed.

In order to set the number of points to be constant for a specific bone contour, a sampling frequency must be chosen to be higher than the Nyquist rate, to insure no loss of important shape detail.

Using the database of normal image contours, Fourier analysis is applied on the contour distance function (Figure 39, Figure 40, Figure 41). From the amplitude spectrum, the cutoff frequency  $f_c$  is chosen (Figure 42), and the sampling frequency  $f_s$  is chosen such that;

$$f_s = 2 * f_c + \tau$$

Where  $\tau > 0$  indicates a tolerance factor to accommodate for high curvature bone deformity, as in the case of osteophytes.

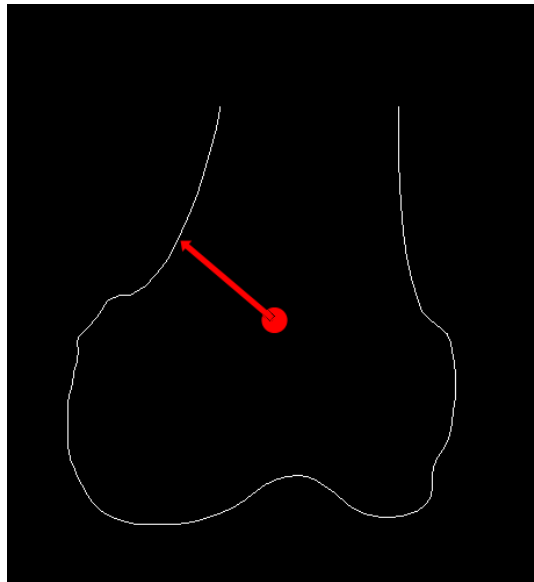


Figure 39 Image showing a distal femur contour with the centroid marked in red, and the arrow highlighting the centroid distance

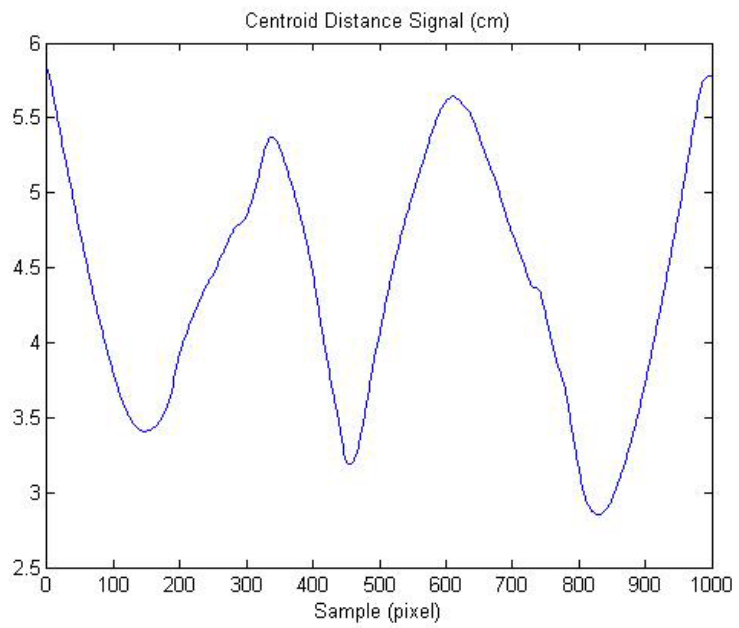


Figure 40 Graph showing the centroid distance function

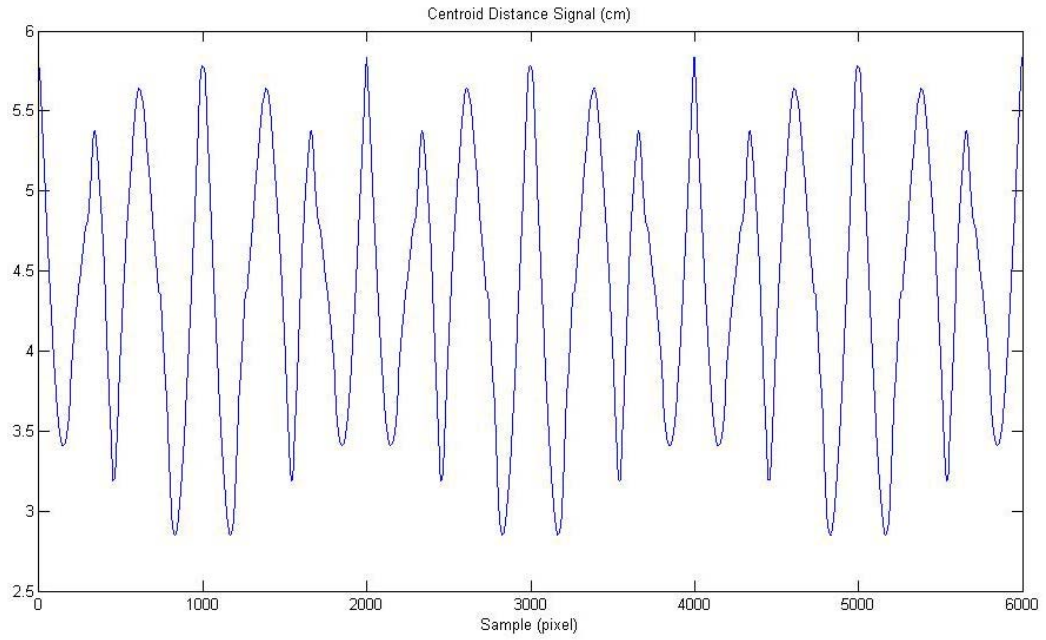


Figure 41 Graph showing the repeated centroid distance function to be used in Fourier analysis

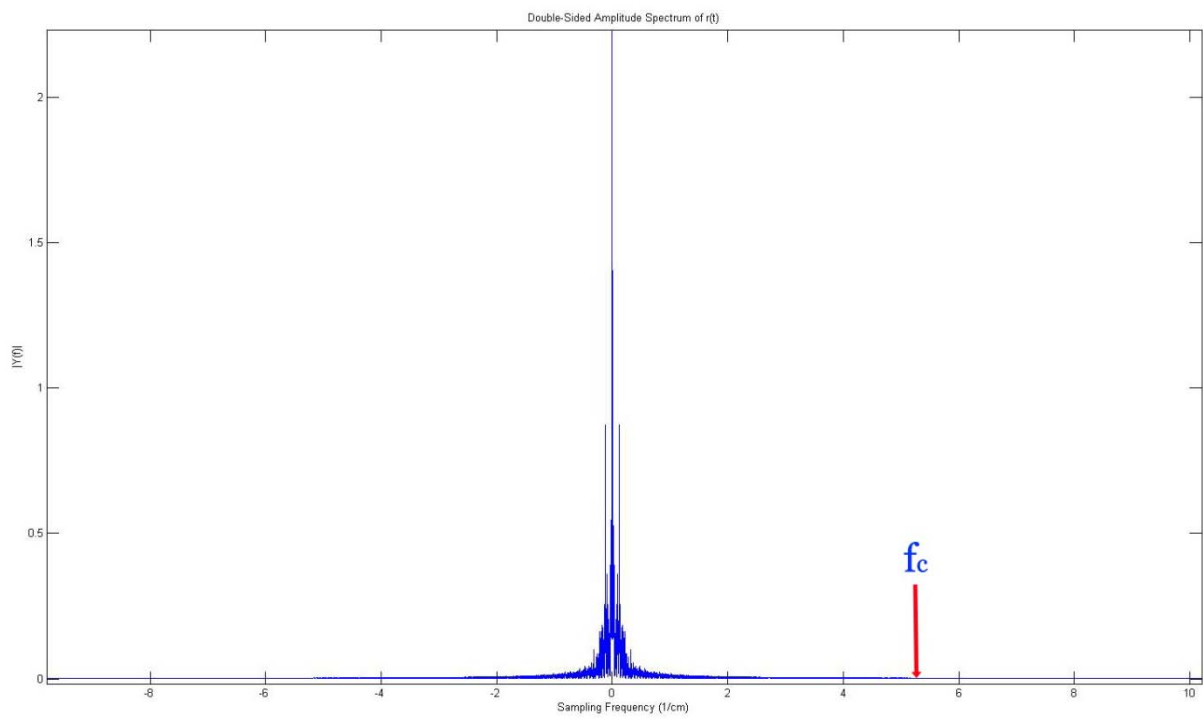


Figure 42 Fourier spectrum of the centroid distance function, showing the cutoff frequency used to select the sampling frequency

Sampling is done using the equal arclength sampling method, which insures the distance between two consecutive points is kept constant. This has the advantage of unit speed of motion along the shape boundary [45], as opposed to other sampling methods like equal number of points sampling and equal angle sampling [46].

#### *Translation and Rotation Normalization*

Translation and rotation of the contours are normalized using Procrustes Analysis and described in [47].

##### **2.4.3.1.1 Contour region extraction and identification**

This module aims at giving anatomical reference to different sub contours. The hypothesis is that, given that the 3D shape of a bone can be subdivided into different parts having unique geometric features, the projection of these subdivisions would reflect such geometric properties.

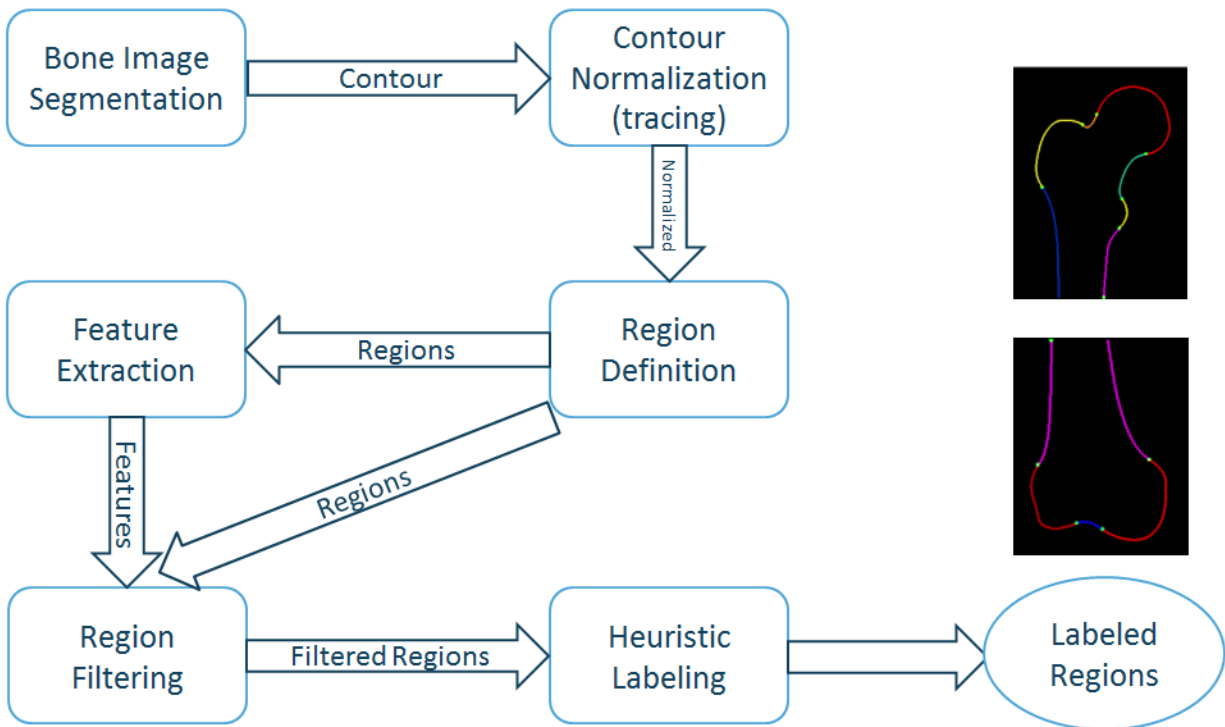


Figure 43: Flowchart showing contour region extraction and Identification

Subdividing a contour into a number of regions requires the existence of separation criteria that uniquely identifies the limits of every region. In computer vision applications, separation criteria are usually lines or corners. In anatomical contours, however, such sharp contour features do not exist due to the smooth nature of anatomical objects.

Nevertheless, examining the curvature of bone contours, a correlation has been found between anatomical structures and contour curvature. For instance, the femoral head is a highly spherical region that produces convex spherical projection. The femoral neck on the



other side produces two concave sub contours. In order to accurately separate the two regions from the proximal femur contour, the following definitions should apply;

- **Contour Curvature:** The contour curvature is the rate by which the tangent to the contour at a specific point rotates. Specifically,

$$\kappa(n) = \frac{d\theta}{ds} = \frac{\dot{x}(n)\ddot{y}(n) - \dot{y}(n)\ddot{x}(n)}{(\dot{x}(n)^2 + \dot{y}(n)^2)^{\frac{3}{2}}}$$

- **Inflection point:** An Inflection Point is a point in the contour where the curvature convexity changes.
- **Contour region:** A contour region is a subset of a contour enclosed between two inflection points.

Figure 44 shows how the inflection points can successfully separate different contour regions.

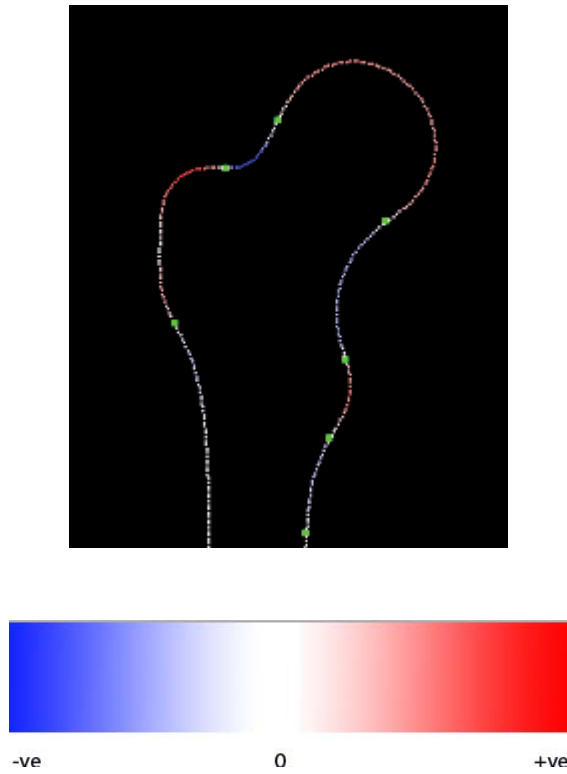


Figure 44: Proximal femur contour showing regions defined based on inflection points. The color of the contour points indicate their curvature.

In practice, due to the discrete nature of contour pixels, and possible contour noise, the number of existing noise inflection points can be a limiting factor for the usability of this method (Figure 45).

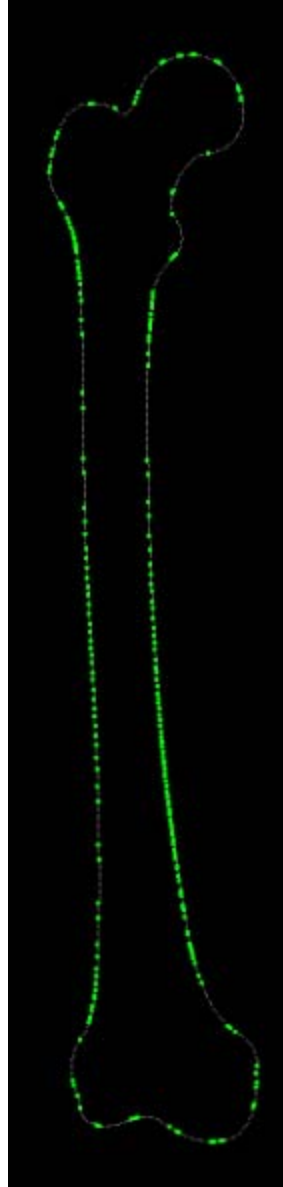


Figure 45: Noise inflection points on femur contour

The solution for such a problem can be borrowed from the field of signal processing. Given that the contour can be treated as a signal  $H(x)$ , the signal can be smoothed by convoluting it with a Gaussian signal  $g(x)$ .

Specifically,

$$H(x) = f(x) * g(x)$$

where,

$$g(x) = \frac{1}{\sqrt{2\pi}\sigma} e^{-\frac{(x-\mu)^2}{2\sigma^2}}$$

The choice of the variance of the Gaussian signal dictates how the degree of smoothing and the filtering out of noisy inflection points. Figure 46 shows the same contour after different levels of smoothing.

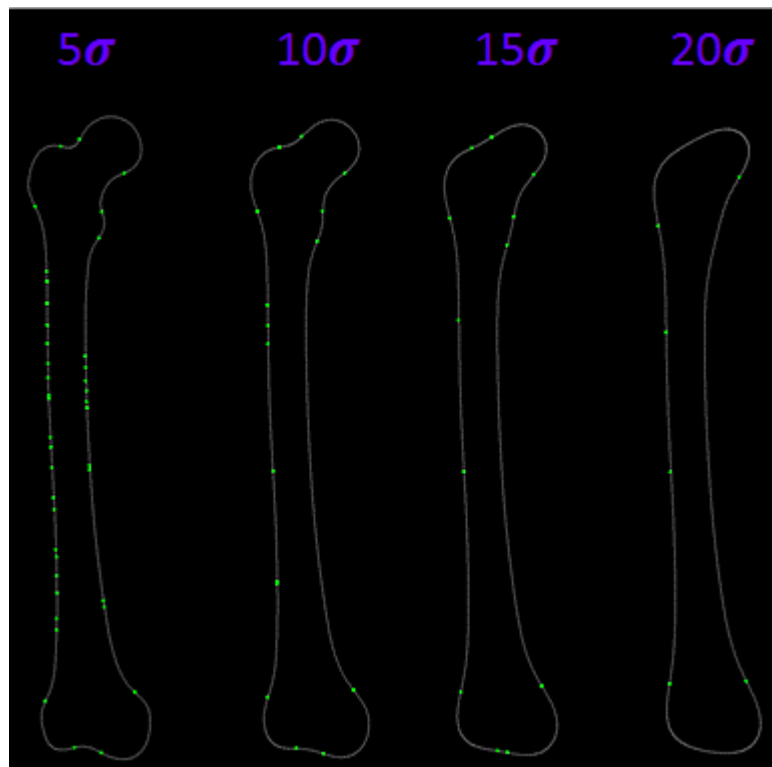


Figure 46: Femur contour smoothed at different Gaussian variances showing inflection points in green.

This shows how excessive smoothing can eradicate important contour features, while some “uninteresting” inflection points may still exist. This raises the need for a well-defined methodology that minimizes smoothing to a limit that preserves the contour shape, while eliminating maximum noisy inflections.

*The Curvature Scale Space (CSS) representation*

The Curvature Scale Space image is a visual mapping for inflection points as Gaussian filter width increases [48]. Figure 47 shows a sample CSS image. Every white point represents an inflection point. As the variance increases, the number of inflection points decreases. Every arc shape represents a contour sub region. The tip of the arc defines the variance at which the region is smoothed out.

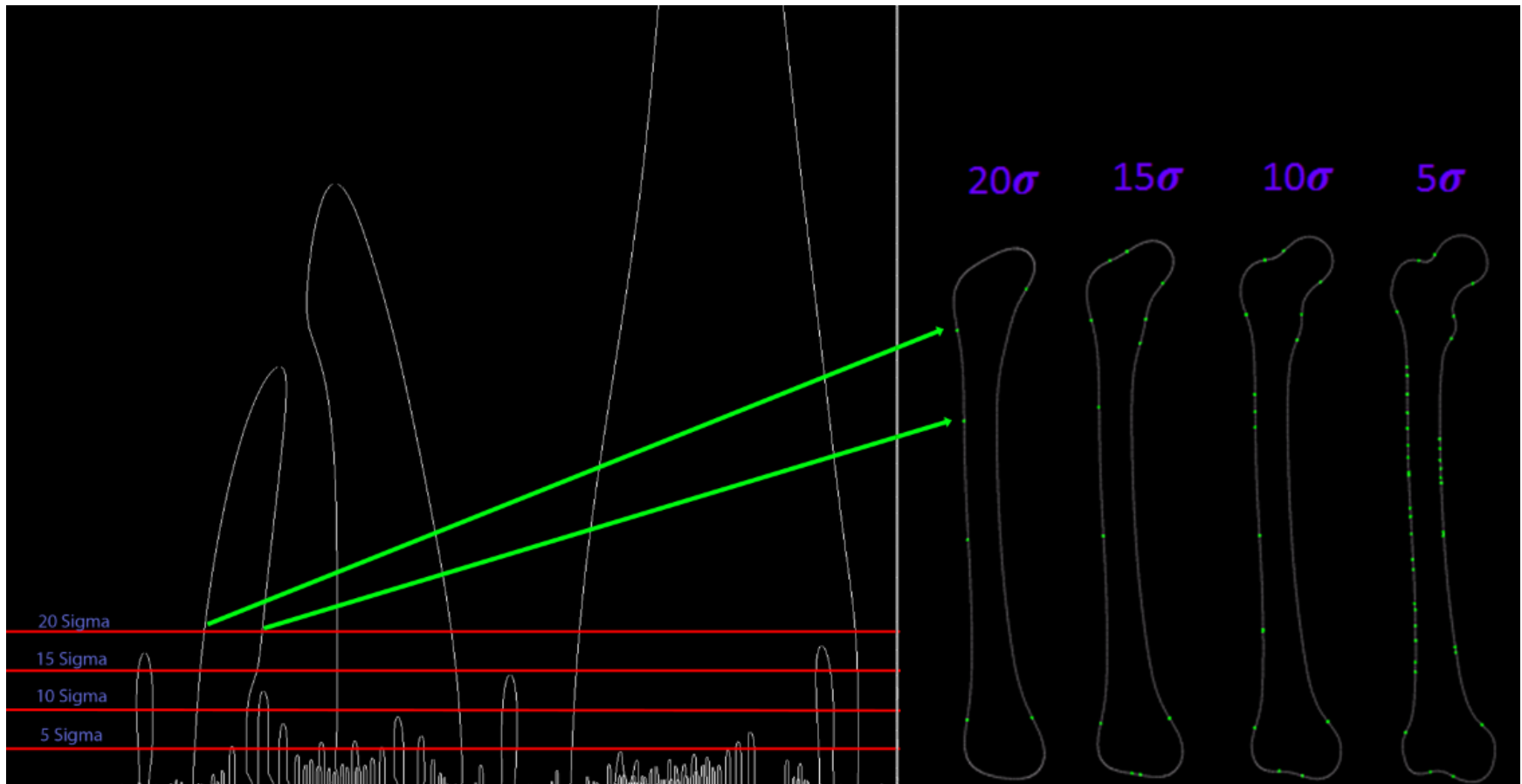


Figure 47: Curvature Scale Space representation of a femur bone showing different smoothing levels inflections

In the CSS image, the narrower the arc, the more indicative that the region it represents is small in the sense of contour length. This fact comes useful when deciding on the variance to use because often times, there will be small regions that would still exist at the required smoothing level. Such small regions will be filtered out by values of contour region features described below.

### *Region Filtering*

Insignificant regions are filtered out by setting a cut-off level for both the chord distance and the region area. The chord distance can be defined as the distance between the starting and ending point of a contour region. It is calculated by;

$$\text{Chord Distance} = \sqrt{(x_N - x_1)^2 + (y_N - y_1)^2}$$

The region area is the area encompassed by the contour sub region. The region is assumed closed by joining the first and last points of the sub contour. It is calculated from the equation;

$$\text{Area} = \frac{1}{2} \left| \sum_{i=1}^N (x_i y_{i+1} - x_{i+1} y_i) \right|$$

Figure 48 shows the results of the filtering stage on the full femur for smoothing variance = 5.

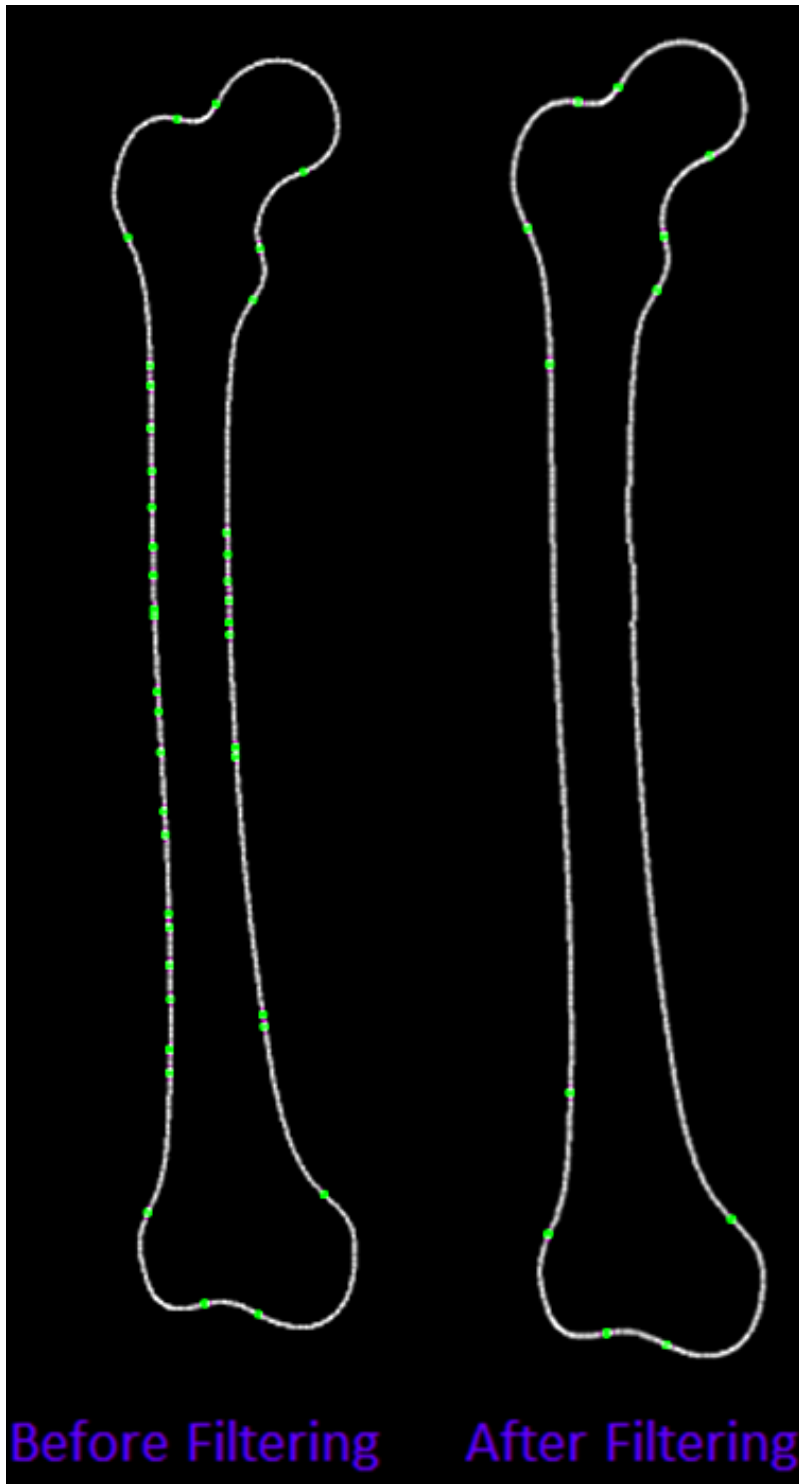


Figure 48: Region filtering effect



### Heuristic Labeling

After the contour is filtered of noisy inflection points, the goal is to identify the following regions (Figure 49);

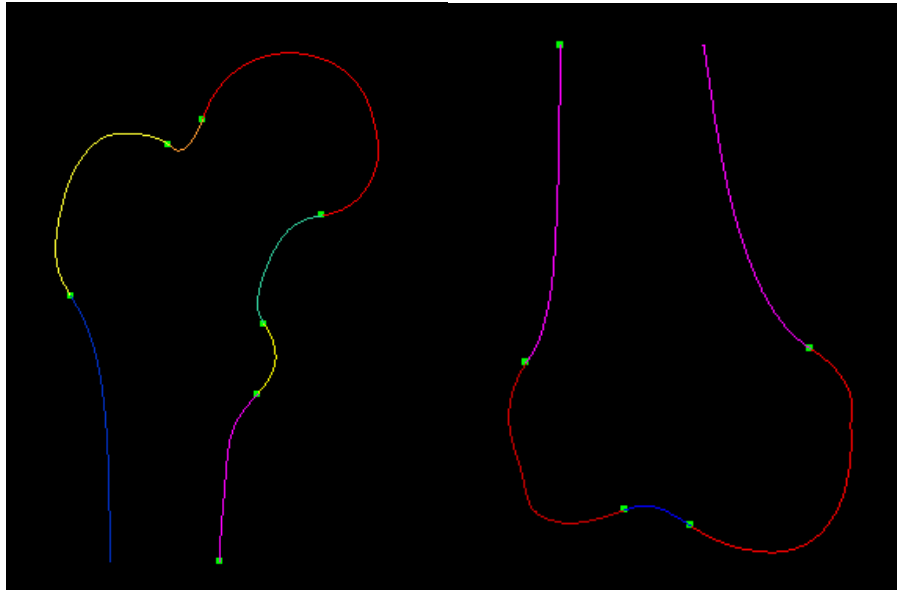


Figure 49: Labeled Contour Regions. Right: Proximal Femur. Left: Distal Femur

- **Femoral Head:** This is identified as being the most circular region. A good indicative of circularity, is the Circularity Ratio, which is calculated by dividing the variance by the mean of the radial distance from the centroid.

$$CV = \frac{\sigma_r}{\mu_r}$$

Where

$$\mu_r = \frac{1}{N} \sum_{i=1}^N d_i$$

$$\sigma_r = \sqrt{\frac{1}{N} \sum_{i=1}^N (d_i - \mu_r)^2}$$

$$d_i = ([x_i - x_c]^2 + [y_i - y_c]^2)^{\frac{1}{2}}$$

$$x_c = \frac{1}{N} \sum_{t=0}^{N-1} x(t), \quad y_c = \frac{1}{N} \sum_{t=0}^{N-1} y(t)$$

- **Distal neck:** This is the concave region following the femoral head.
- **Proximal Neck:** This is the concave region preceding the femoral head.
- **Lesser Trochanter:** This is the convex region following the distal neck.
- **Greater Trochanter:** This is the convex region preceding the proximal neck.
- **Medial Proximal Shaft:** Follows the lesser trochanter.
- **Lateral Proximal Shaft:** Precedes the greater trochanter.
- **Medial Condyle and Lateral Condyle:** Most circular regions at the distal end of the bone.
- **Distal Groove:** Separates the two condyles.

#### 2.4.3.1.2 Extracted Features

Using the extracted features, the global shape features (such as Fourier descriptors), region specific features such as circularity, eccentricity, and accumulated curvature, and inter-region features such as Neck angle will be extracted (Figure 50). Following, the list of extracted featured will be described.

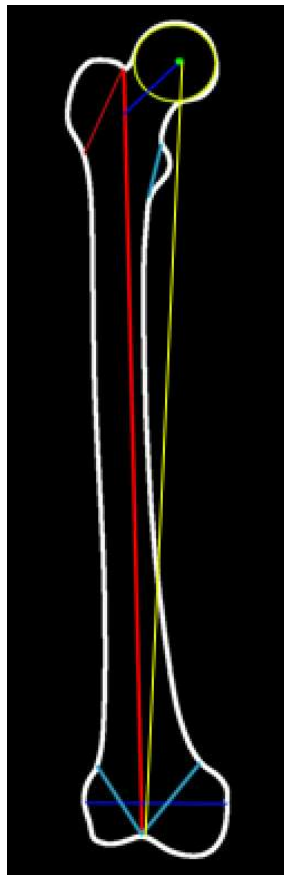


Figure 50 Image showing how some features are described.

### Fourier Descriptors

Zheng et al. showed in [46] that using FDs derived from the centroid distance signature is significantly better than that using FDs derived from the other signatures. Given a contours centroid  $(x_c, y_c)$ , where;

$$x_c = \frac{1}{N} \sum_{t=0}^{N-1} x(t), \quad y_c = \frac{1}{N} \sum_{t=0}^{N-1} y(t)$$

The centroid distance function  $r(t)$  can be calculated as;

$$r(t) = ([x(t) - x_c]^2 + [y(t) - y_c]^2)^{\frac{1}{2}}$$

Fourier descriptors  $a_n$  can then be calculated using  $r(t)$  using the following equation;

$$a_n = \frac{1}{N} \sum_{t=0}^{N-1} r(t) \exp\left(\frac{-j2\pi nt}{N}\right), n = 0, 1, \dots, N - 1$$

### Femoral head center

This is defined as the center of gravity  $(C_x, C_y)$  of the femoral head region. The center of gravity can be calculated as:

$$C_x = \frac{1}{6A} \sum_{i=1}^N (x_i + x_{i+1})(x_i y_{i+1} - x_{i+1} y_i)$$

$$C_y = \frac{1}{6A} \sum_{i=1}^N (y_i + y_{i+1})(x_i y_{i+1} - x_{i+1} y_i)$$

### *Neck Axis*

This is defined as the center line of the two neck regions, starting from the femoral head center.

### *Neck Angle*

This is defined as the angle between the Neck axis and the anatomical axis

### *Anatomical Axis*

This is defined by the line joining the center of the proximal neck region to the center of the distal groove region.

### *Mechanical Axis*

This is defined as the line joining the femoral head center, to the center of the distal groove region.

### *Circularity*

Circularity ratio is the circle variance. It can be calculated from:

$$C_{va} = \frac{\sigma_R}{\mu_R}$$

Where  $\mu_R = \frac{1}{N} \sum_{i=1}^{N-1} d_i$  and  $\sigma_R = \sqrt{\frac{1}{N} \sum_{i=1}^{N-1} (d_i - \mu_R)^2}$

$$d_i = \sqrt{(x_i - C_x)^2 + (y_i - C_y)^2}$$

This is calculated for all extracted contour regions.

### *Eccentricity*

It is the ratio of the length of major axis to the length of minor axis. It is calculated for all extracted contour regions from the ratio between the second to the first principle axis.

### *Average Bending Energy*

This is calculated for all extracted contour regions from:

$$BE = \frac{1}{N} \sum_{s=0}^{N-1} K(s)^2$$

Where  $K(s)$  is the curvature function and  $s$  is the arclength parameter

### **2.4.3.2 Feature Selection**

Pose parameters should be estimated using features that are highly correlated to them. In this section, we investigate the best features that can indicate the different pose parameter values. Given the large number of extracted features, these features will be filtered using the Fisher Discriminant score  $F_f$  as in [49]. The score discovers which features are most affected by the change in bone rotation by calculating the ratio of variance of class means to the mean of within-class variances. This would result in an objective evaluation for each of the features' effectiveness as a pose indicator.

$$F_f = \frac{1}{N} \sum_{c=1}^N \frac{(\mu_f - \mu_{f,c})^2}{\sigma_{f,c}^2}$$

### 2.4.3.3 Pose Learning

For every image in the synthetic image dataset, a vector containing the values of the most significant features is created, associated with the rotational pose used to create the synthetic image.

$$\begin{aligned} [f_1, f_2, f_3, \dots, f_n] &\xrightarrow{1} [R_x, R_y, R_z] \\ [f_1, f_2, f_3, \dots, f_n] &\xrightarrow{2} [R_x, R_y, R_z] \\ [f_1, f_2, f_3, \dots, f_n] &\xrightarrow{3} [R_x, R_y, R_z] \\ &\cdot \\ &\cdot \\ &\cdot \\ [f_1, f_2, f_3, \dots, f_n] &\xrightarrow{N-1} [R_x, R_y, R_z] \\ [f_1, f_2, f_3, \dots, f_n] &\xrightarrow{N} [R_x, R_y, R_z] \end{aligned}$$

This would comprise a learning that can be entered into a machine learning algorithm. Such a problem would require a non-linear classifier. In this work, the Support Vector Machine (SVM) clustering algorithm was used in association with a Gaussian radial basis function kernel.

For any new image in the x-ray dataset, the extracted contour goes into the feature extraction module to extract the specified significant features. The features are now entered as an input to the SVM classifier, which gives an accurate guess for the rotational pose parameters.

#### 2.4.3.4 Translation Extraction

In this section, the 3D translation that translates the bone from the atlas space (centered around the origin) to the simulated scene's correct location. This is done by automatically extracting the origin point location on the image dataset(Figure 51).

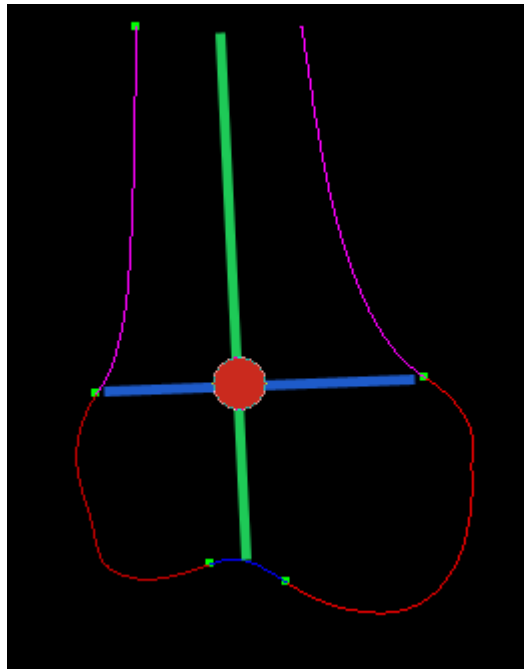


Figure 51 Origin point (Red) extracted using extracted features

These point correspondences are used to optimize a point location lying on the line joining the camera to the origin point on one image to overlap the corresponding point on the other image, given epipolar constraints. Optimization was done using Powell's method. The 3D translation for other views is then calculated using the relative transformation between images. Figure 52 show how the origin points are extracted and used for bone placement.



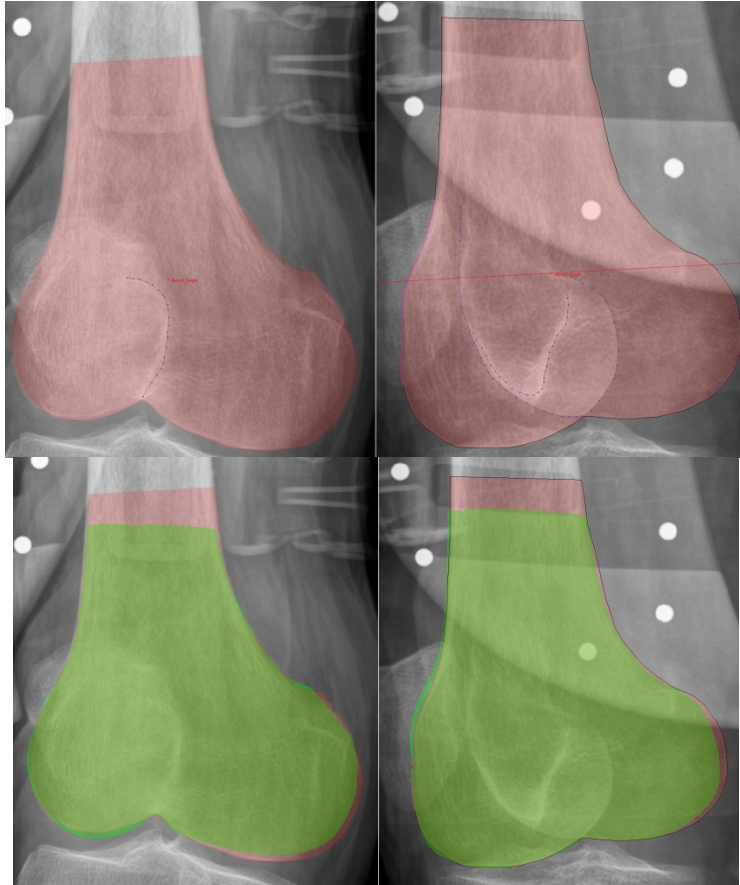


Figure 52 Top: Corresponding origin points on the AP and LAT images. Bottom: Initialized bone placement in green.

#### 2.4.4 Scale initialization

Since the bones are now placed at the correct location, the bone scale can now be estimated. The scale factor is calculated using the ratio between the size of the projected vs. segmented contours. Contour size was calculated using the Frobenius norm. Isotropic scaling of the template by the extracted scaling factor produces a bone size similar to the patient's (Figure 53).

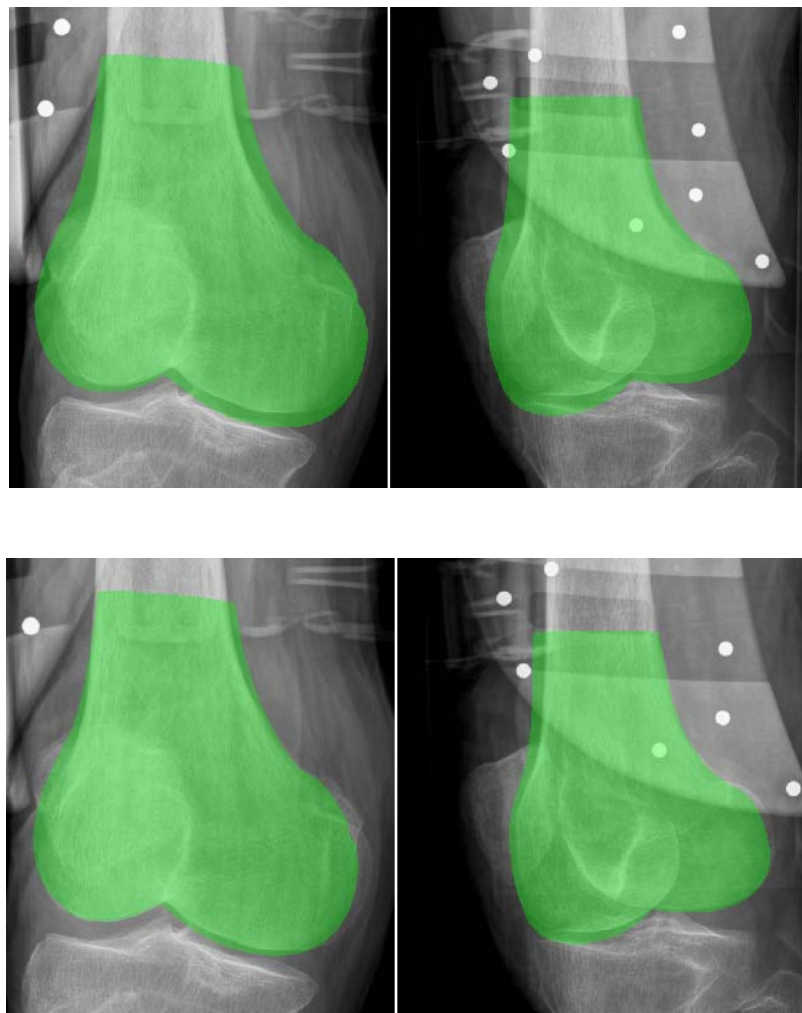


Figure 53 Top: Before scaling, Bottom: After scaling

## 2.5. Model Deformation

In order for the scaled template model, placed at the correct pose to fit the image features, its shape would need to be manipulated. This is done using the following steps (Figure 54)

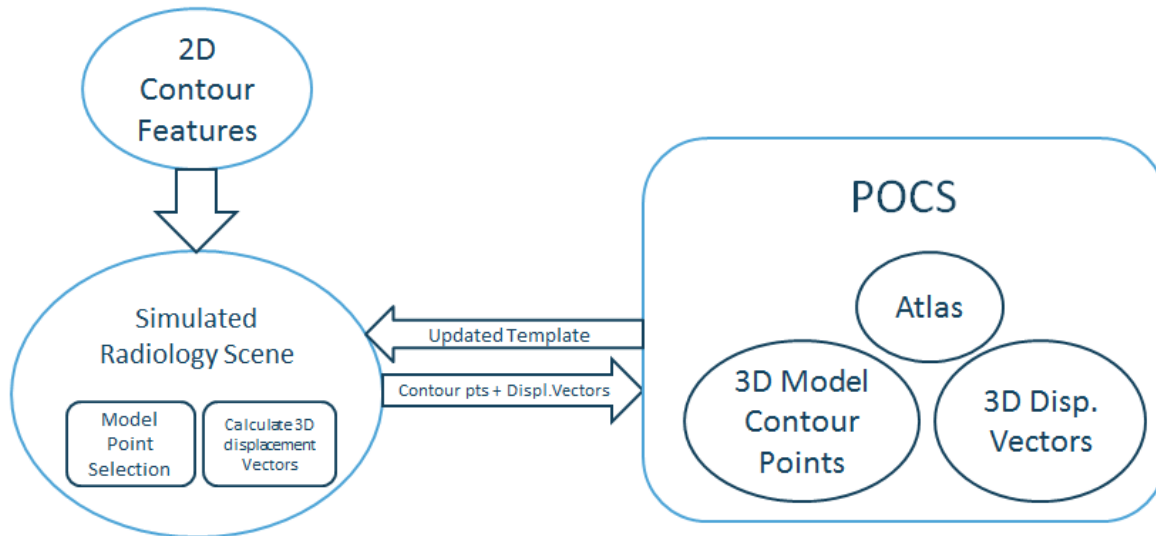


Figure 54: Block Diagram for the bone morphing process

### 2.5.1. Build 3D Simulated Scene

The 3D reconstruction algorithm is based on perspective rendering simulation. The input is the set of segmented images and their corresponding bone poses. The number of images and the variety of projection poses indicates the amount of information that can be obtained about the bone shape, hence the accuracy of the output. For each of the input images, a graphical rebuild of the radiological scene used to take the image is done. The x-ray source is represented by a perspective camera setup to simulate the radiological beam divergence. Within the

camera's field of view, a template bone model is placed at a pose mimicking the actual bone's pose within the radiological scene.

### 2.5.2. Model Point selection

Given the simulated scenes, rays are generated between the x-ray source location and all the segmented image contour points (Figure 55).

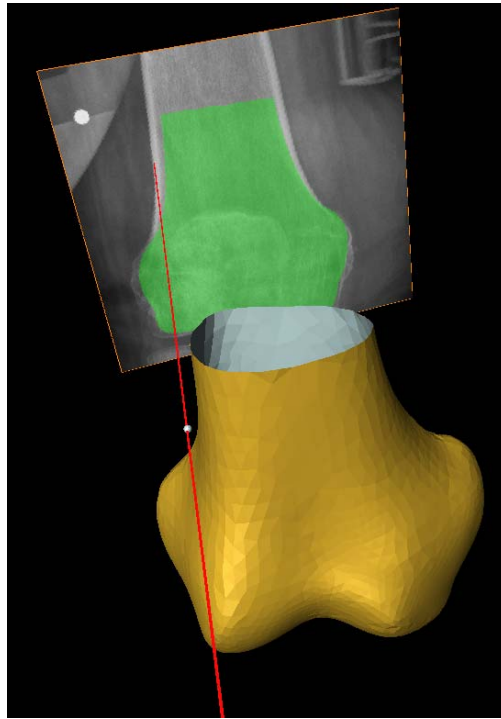


Figure 55 Image showing 3D mapping of an image contour point. The red line is an example ray joining a contour point to the x-ray source location. The bead on the red line is the closest line point to the 3D model, and the shortest distance between the bead and the model indicates the 3D fitting error.

This transforms the model fitting problem from 3D-to-2D to 3D-to-3D problem. The point(s) that would need to be morphed, for the template model to accurately fit the image features are defined using two criteria (Figure 56);

- a) The vertex should have a distance less than  $d$  to the ray.
- b) The angle between the vertex normal and the ray should be greater than  $(90 - \alpha)$ . The angle between the vertex normal and the image normal should be greater than  $(90 - \alpha)$

The values of the distance  $d$  and angle  $\alpha$  would start with a larger value, to allow for a larger number of points to move, leading to a smoother deformation. The values would then decrease at every iteration for finer local deformation.

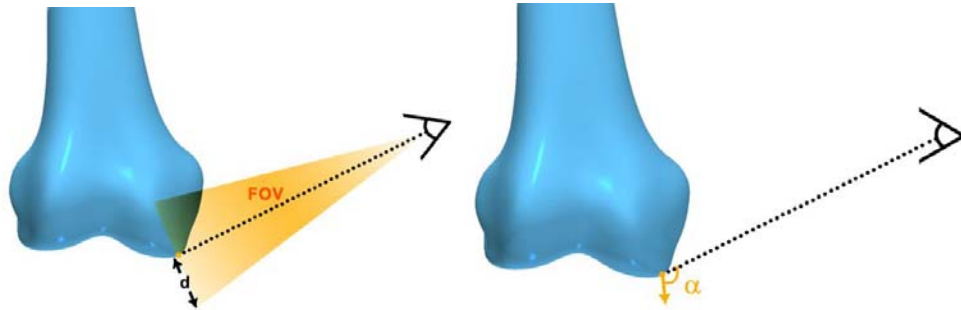


Figure 56 Left: Distance selection criterion. Right: Angle selection criterion

Figure 57 shows an example of the selected points.

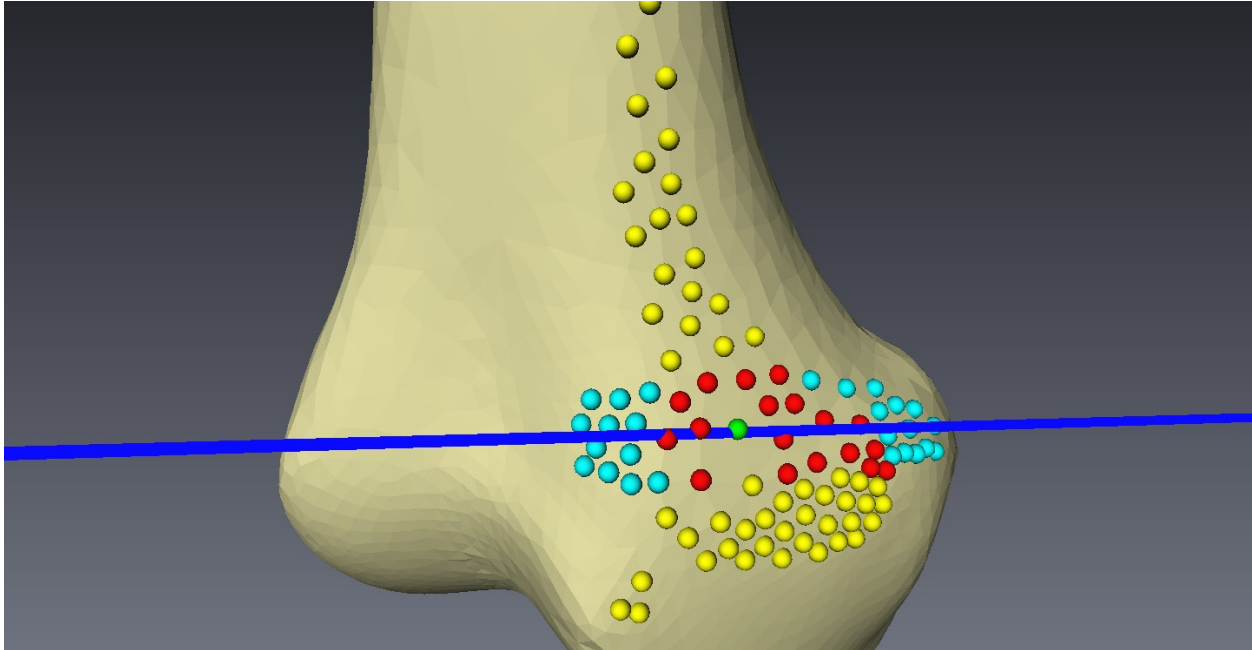


Figure 57 Model point selection. Alpha points (yellow) and distance points (blue). Intersection is in red. Here alpha = 10 degrees, d = 5 mm.

### 2.5.3. Calculation of 3D Displacement Vectors

For every ray, selected points are morphed by moving them in a direction normal to the model surface. The distance moved is the closest point's distance to the ray. The result is that every 3D vertex  $V_c$  contributing to the projection silhouette is translated in a direction that eliminates the 2D projection error, while being parallel to the image plane. This produces a projection  $V_c'$  that overlaps the x-ray image bone contour.

The correspondence is based on the fact that the projection silhouette point would always be the result of the projection of points and edges of the template bone model. Those points and edges are also tangential to the surface of the radiation cone. The assumption is that

there is only one shape and pose tuple that would allow such constrains. That assumption is generally accepted in literature [25].

#### 2.5.4. Deformation Using Projection on Convex Sets (POCS)

Given the template model, and the deformation needed by the silhouette vertices, the problem becomes a 3D/3D optimization problem. The target for such optimization is to morph the initial template, in order to create a 3D bone that follows the new silhouette vertices location requirements.

Instead of using traditional gradient-based or stochastic optimization techniques that might be slow and do not guarantee optimum convergence, the POCS (alternating Projection on Convex Hulls) method [50] is proposed. Given the domain of the problem, this method is well-suited to quickly and uniquely find the best shape that is consistent with both the statistical atlas as well as the generated point cloud in a systematic consistent fashion. POCS is a powerful tool that has been used successfully for many signal and image restoration and synthesis problems. It is particularly useful in problems which can be regularized by imposing possibly nonlinear convex constraints on the solution set. Iteratively projecting onto these convex sets results in a solution that is consistent with all the desired properties.

Given any two vectors  $\vec{\mu}_1$  and  $\vec{\mu}_2$  belonging to the set  $A$ . The set  $A$  is convex if

$$\alpha\vec{\mu}_1 + (1 - \alpha)\vec{\mu}_2 \in A \quad \text{where } 0 \leq \alpha \leq 1$$

In other words, the line segment joining  $\vec{\mu}_1$  and  $\vec{\mu}_2$  should be totally contained in  $A$ . If any portion of the segment connecting two vectors lies outside of the set, the set is not convex.

For a vector  $\vec{v}$ , if  $\vec{v} \in A$ , then its projection onto  $A$  is  $\vec{v}$ . If  $\vec{v} \notin A$ , the projection onto  $A$  is the unique vector  $\vec{\mu} \in A$  such that the distance between  $\vec{\mu}$  and  $\vec{v}$  is the minimum. The most useful aspect of POCS is that, given two or more convex sets with nonempty intersection, alternately projecting among the sets will converge to a point included in the intersection. The actual point of convergence is dependent on the initial vector.

If the two convex sets do not intersect, convergence is to a limit cycle that is a mean square solution to the problem (Figure 58). Specifically, the cycle is between points in each set that are closest in the mean-square sense to the other set[51].



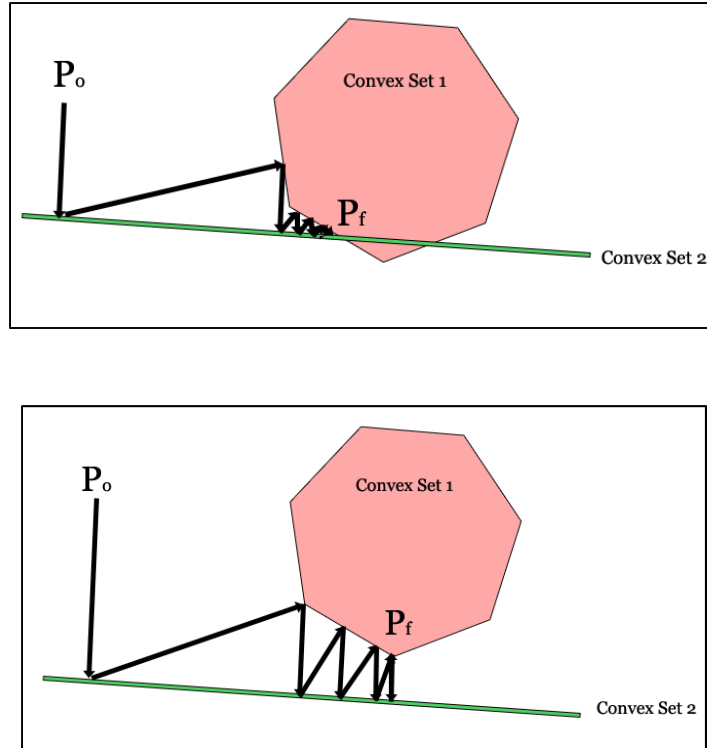


Figure 58 Images showing POCS convergence. Top: If the two sets intersect, the convergence is to an intersection point. Bottom: if the two sets do not intersect, convergence is to a limit cycle that minimizes the distance between the two sets.

In the current problem domain, there are two convex sets:

- 1- The set  $A$  of all bones that belong to the statistical bone atlas. Since the PCA-based atlas has the property of being linearly interpolative onto orthogonal basis, this set would form a hypercubic set, which is convex.
- 2- The set  $B$  of all bones that have constrained values equal to  $V'_c$  for a selected number of vertices. Those vertices are those for which we see corresponding points on the projective image contour.

$$B = \{b | V'_c \in b\}$$

It is assumed that bone following the second set criterion is unique, which comprises a special case for a convex set (single element). If the assumption does not hold, any element of set  $B$  would suffice for the POCS iteration, since the projection back to set  $A$  would guarantee a valid bone with the desired contour properties.

Projection of an element of set  $A$  onto the second set is done by translating the contour vertices as described in previous section. This results in a deformed bone (Figure 59).

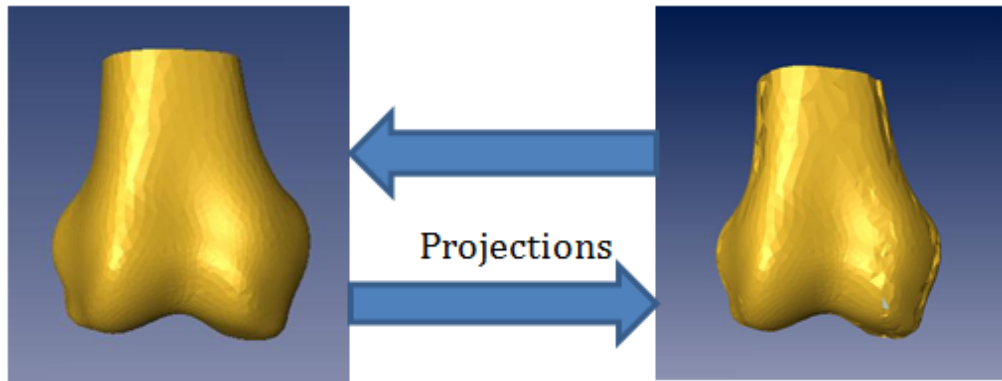


Figure 59 Image showing alternating projections. Right: Deformed bone after projecting onto the set  $B$ . Left: Same bone after projecting back to set  $A$ .

Projection on the first set is done by projecting the deformed bone onto the atlas eigen vectors to extract the new eigen weights.

$$b_k = \sum_{m=1}^n (T_m - \overline{T_m}) * p_m$$

After that, the new deformed template would be obtained by reconstructing a bone form these weights.

$$T_i = \bar{T} + \sum_{k=1}^n b_k p_k$$

Where  $\bar{T}$  is the mean atlas bone,  $b_k$  is the set of PCA weights, and  $p_k$  is the eigen vectors of the covariance matrix of the atlas

$$Cov = \sum (T_i - \bar{T})(T_i - \bar{T})^T$$

Alternating projections would continue, until convergence using relative RMS as an indicator. The result is the final patient-specific bone model.

### 2.5.5 Cartilage Estimation

After reconstructing the bone models, cartilage can be estimated from the knee joint bones, and added to the models as explained in [53].

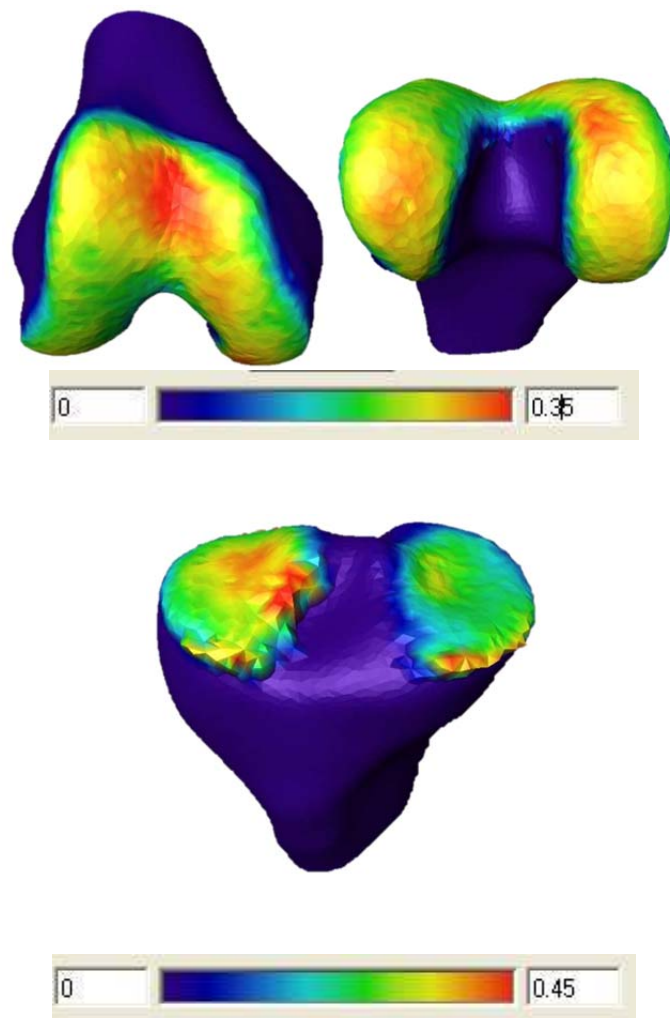


Figure 60 Thickness distance map of added cartilage. Top: Femur, Bottom: Tibia

## Chapter 3: Verification and Results

---

In this chapter verification studies done on cadaveric and live patient cases to assess the accuracy of the bone reconstruction system, and its feasibility to be used within surgical applications. These results can be considered promising, as suggested by [54], that the average reconstruction error for surgical applications should be around 1.5 mm and the maximum error to be between 2-3 mm. They are also superior to results obtained in the literature.

### 3.1 Fitting RMS Error Assessment

In an attempt to assess the quality of fitting to the x-ray extracted contours, a localized 3D RMS distance error calculation was done between the vertices of the final reconstructed bone, and the two 3D contours extracted from the AP and Lateral x-ray images as shown in Figure 61. The 3D fitting points are points corresponding to the lines joining the x-ray image contour points, to the x-ray source location, that have the closest distance to the model vertices. Case results are shown in Table 4 and Table 5.

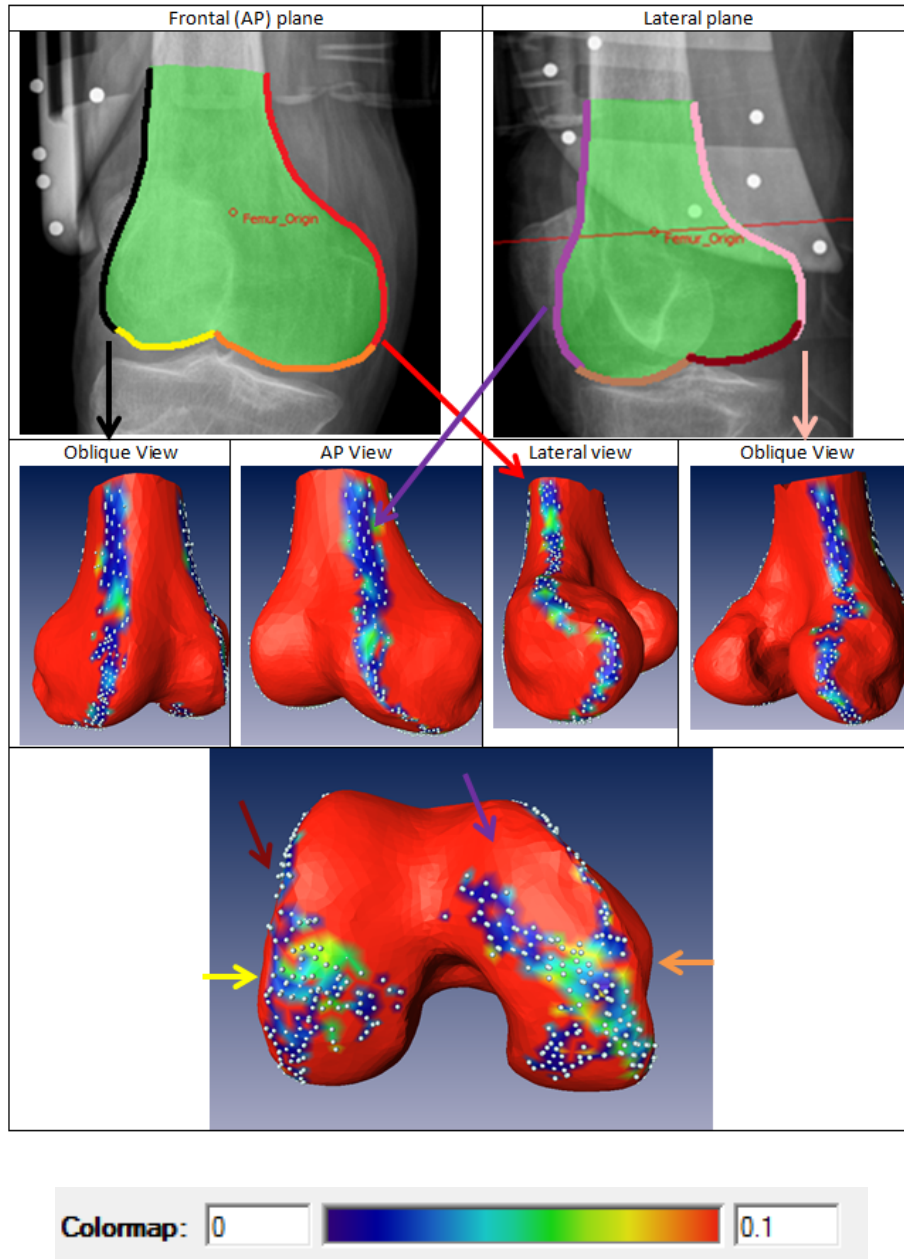


Figure 61 Top: X-ray images with the reconstructed bone projected. Bottom: Reconstructed 3D model showing beads representing x-ray extracted 3D fitting points. The colormap on the bone shows the distance to the beads in cm.

Table 4 Fitting RMSE between femur x-ray reconstructions utilizing the scale independent atlas and manual segmentations.

Case	Fitting RMSE (mm)
751 – Right	0.505
765 – Left	0.567
772 – Left	0.449
778 – Right	0.457

Table 5 Fitting Root Mean Square Error between tibia x-ray reconstructions utilizing the scale independent atlas and manual segmentations.

Case	Fitting RMSE (mm)
751 – Right	0.651
765 – Left	0.748
772 – Left	0.518
778 – Right	0.866

### 3.2 Mechanical Axis Calculation Accuracy Assessment

The mechanical axis is important for clinical studies. In order to assess the accuracy of the mechanical axis registration in case of short film x-ray images, a study was done as follows.

- a- The Extreme Mechanical Axis Points (EAP) were calculated in a manner similar to what was explained in section 2.4.3.4. (Figure 62)

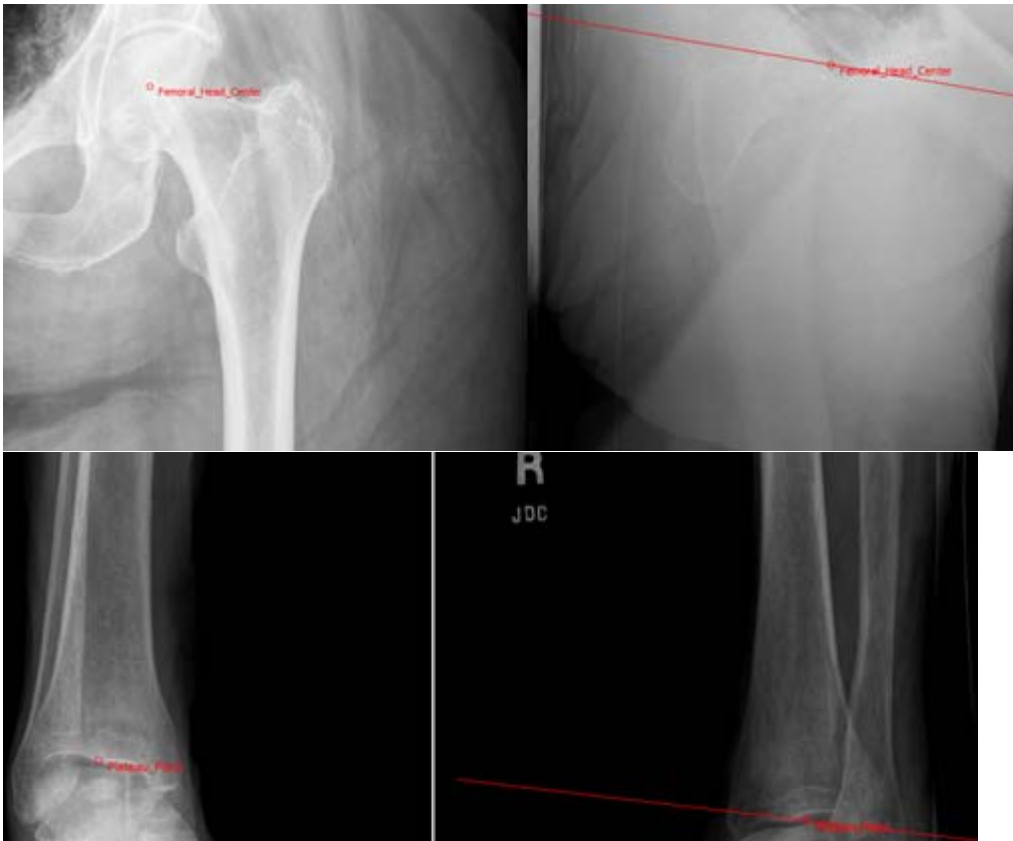


Figure 62 EAP Calculation. Top: Femoral Head center. Bottom: Ankle Center

- b- For each of the test cases, complete x-ray reconstruction will be done 3 times, in order to reconstruct the knee bones, and to extract the mechanical axes' points.



- c- Rigid surface registration of the corresponding MRI and X-Ray bones was done by Centroid alignment, followed by alignment.
- d- The obtained transformation matrix will be used to transform the MRI EAP to the x-ray bone space.
- e- The x-ray bone's mechanical axis entry point was automatically defined using the statistical atlas correspondence. The extracted mechanical axis entry point was used as a Common Axis Point (CAP) to both the axis of MRI and x-ray.
- f- The 3D angle  $\theta$  formed between the two EAPs and the CAP will define the 3D mechanical axis error (Figure 63).
- g- The projection of the 3D angle on the image plane, will define the 2D mechanical axis error. This is important for comparison to clinical 2D measurement systems

Table 6 and Table 7 show the error assessment results.

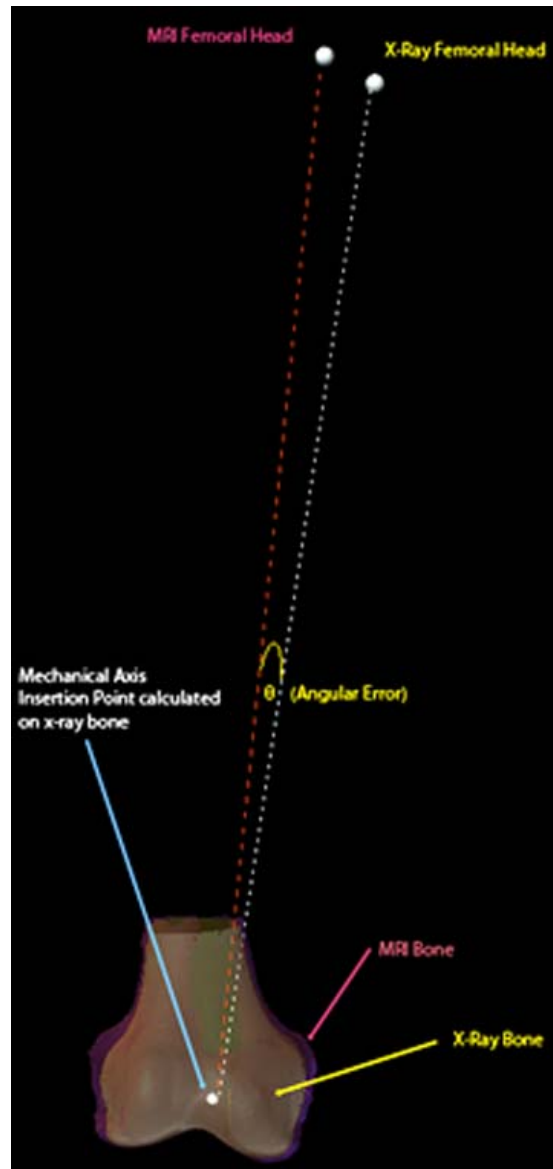


Figure 63 2D and 3D mechanical axis angular error calculation

**Table 6 Femur Mechanical accuracy assessment compared to MRI**

	Femur MA angular error 2D (degrees)	Femur MA angular error 3D (degrees)
<b>Case 751R</b>		
Iteration 1	0.29	1.89
Iteration 2	0.36	1.91
Iteration 3	0.25	1.93
Mean	0.3	1.91
STD	0.05	0.02
<b>Case 765L</b>		
Iteration 1	0.06	2.02
Iteration 2	0.05	2.12
Iteration 3	0.11	2.07
Mean	0.07	2.07
STD	0.03	0.05
<b>Case 751L</b>		
Iteration 1	0.63	0.92
Iteration 2	0.57	0.91
Iteration 3	0.67	0.93
Mean	0.62	0.92
STD	0.05	0.01
<b>Case 778R</b>		
Iteration 1	0.1	1.13
Iteration 2	0.19	1.14
Iteration 3	0.16	1.09
Mean	0.15	1.12
STD	0.05	0.03
<b>Overall Mean</b>	<b>0.29</b>	<b>1.505</b>
<b>Overall STD</b>	<b>0.05</b>	<b>0.03</b>

**Table 7 Tibia Mechanical accuracy assessment compared to MRI**

	Tibia MA 2D angular error (degrees)	Tibia MA 3D angular error (degrees)
<b>Case 751R</b>		
Iteration 1	0.15	2.7
Iteration 2	0.03	2.74
Iteration 3	0.05	2.5
Mean	0.08	2.64
STD	0.06	0.13
<b>Case 765L</b>		
Iteration 1	1.45	1.38
Iteration 2	1.51	1.47
Iteration 3	1.44	1.29
Mean	1.47	1.38
STD	0.04	0.09
<b>Case 751L</b>		
Iteration 1	0.24	2.38
Iteration 2	0.16	2.34
Iteration 3	0.21	2.49
Mean	0.21	2.41
STD	0.04	0.08
<b>Case 778R</b>		
Iteration 1	1.54	2.25
Iteration 2	1.53	2.13
Iteration 3	1.55	2.34
Mean	1.54	2.24
STD	0.01	0.11
<b>Overall Mean</b>	<b>1.07</b>	<b>2.42</b>
<b>Overall STD</b>	<b>0.04</b>	<b>0.1</b>

### 3.3 Femur Reconstruction

Table 8 shows the RMS error assessment of femur reconstruction compared to MRI manually segmented gold standard models for a clinical case (live patient) reconstructed using long film x-rays and 8 cadaveric cases reconstructed using short film x-rays.

**Table 8. Mean Femur RMS error and STD for reconstructions**

Case	Femur Bone		Femur Bone with Cartilage	
	RMSE (mm)	Standard Dev. (mm)	RMSE (mm)	Standard Dev. (mm)
<b>Clinical Case</b>	1.1	0.75	1.25	0.8
<b>342 L</b>	1.16	0.79	1.15	0.74
<b>342 R</b>	1.94	1.26	1.74	1.12
<b>385 R</b>	1.34	0.81	1.46	0.85
<b>385 L</b>	1.22	0.74	1.28	0.76
<b>751 R</b>	0.76	0.455	0.78	0.453
<b>765 R</b>	1.05	0.76	1.17	0.808
<b>778 L</b>	0.76	0.43	0.74	0.46
<b>778 R</b>	1.04	0.612	1.18	0.739
<b>Mean</b>	<b>1.15</b>	<b>0.73</b>	<b>1.19</b>	<b>0.75</b>

Figure 64 shows the signed distance map for the clinical case.

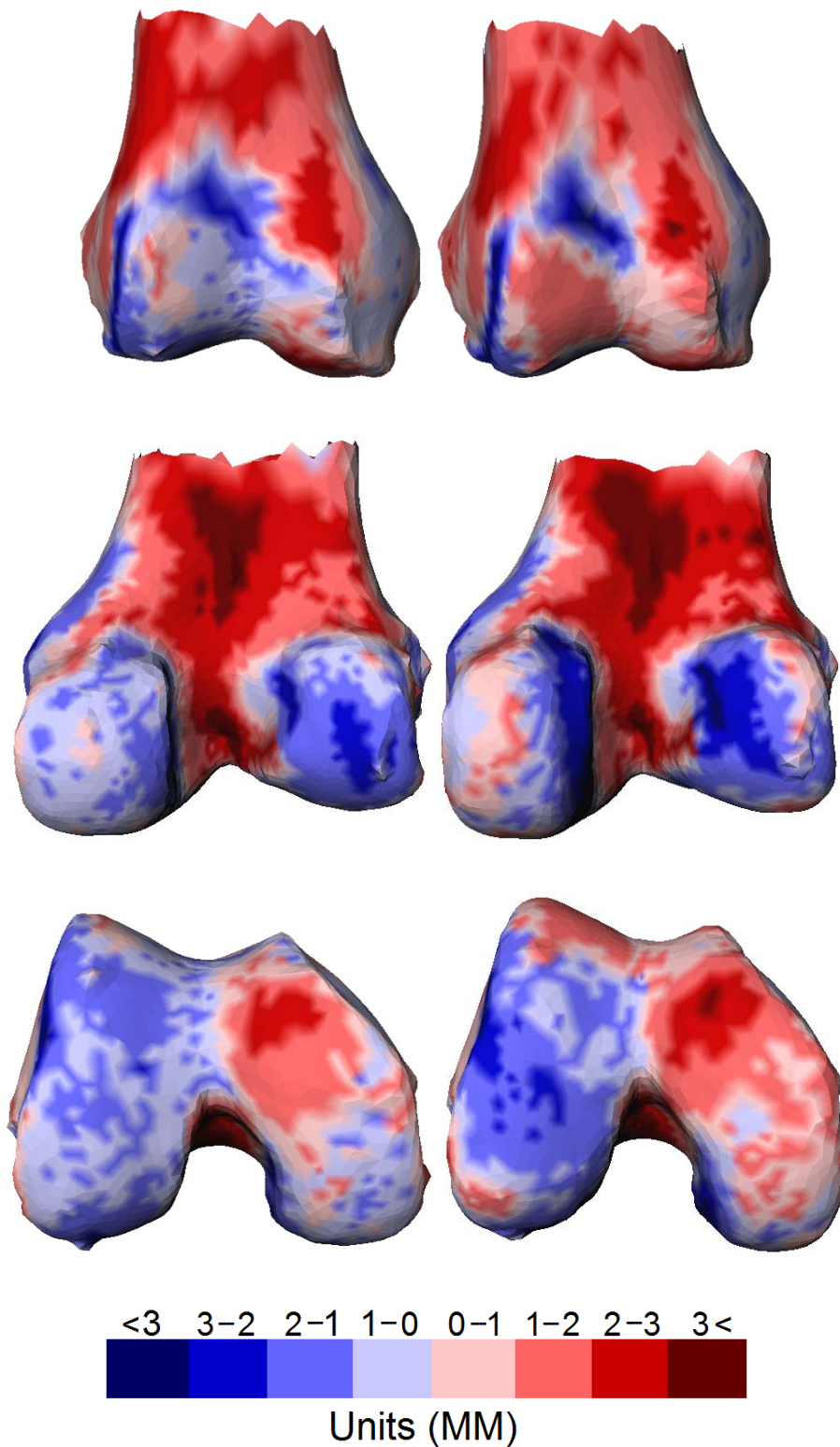


Figure 64. Distal Femur surface distance map between x-ray reconstruction and manual MRI segmentation for the live patient. Right: With estimated cartilage, Left: Without estimated cartilage. Positive values indicate the x-ray reconstruction is larger than the manual segmentation, negative values indicate smaller regions.

### 3.4 Tibia Reconstruction

Table 9 shows the RMS error assessment of femur reconstruction compared to MRI manually segmented gold standard models for a clinical case (live patient) reconstructed using long film x-rays and 8 cadaveric cases reconstructed using short film x-rays.

Table 9. Mean Tibia RMS error and STD for reconstructions

Case	Tibia Bone		Tibia Bone with Cartilage	
	RMSE (mm)	Standard Dev. (mm)	RMSE (mm)	Standard Dev. (mm)
Clinical Case	0.91	0.58	0.91	0.59
342 L	1.05	0.62	1.14	0.7
342 R	0.99	0.61	1	0.68
385 R	1.24	0.8	1.3	0.8
385 L	1.09	0.69	1.09	0.69
751 R	0.81	0.52	0.89	0.55
765 R	1.02	0.68	1.09	0.68
778 L	1.14	0.12	1.11	0.67
778 R	0.97	0.55	0.99	0.62
Mean	<b>1.02</b>	<b>0.57</b>	<b>1.06</b>	<b>0.66</b>

Figure 65 shows the signed distance map for the clinical case.

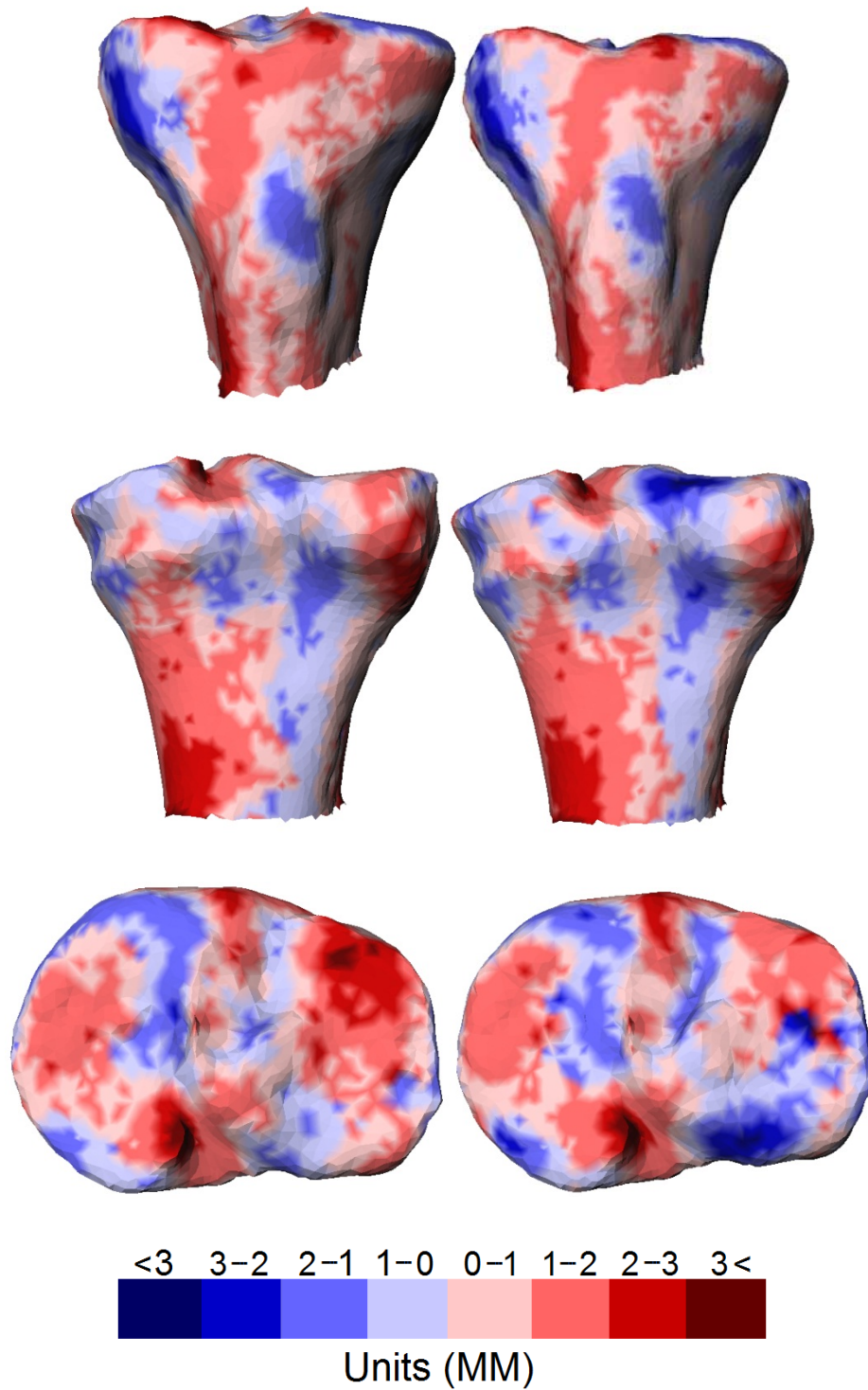


Figure 65. Proximal tibia surface distance map between x-ray reconstruction and manual MRI segmentation for the live patient. Right: With estimated cartilage, Left: Without estimated cartilage. Positive values indicate the x-ray reconstruction is larger than the manual segmentation, negative values indicate smaller regions.



## Chapter 4: Future Work

---

- Automatic bead correspondence matching using brace projection features as a guide.
- Investigate the inclusion of textural features for reconstruction
- Automatic detection of Kellgren-Lawrence (KL) scoring
- Develop a statistical model for bone deformity based on the KL scoring system.
- Add more image views that can provide extra information about hidden areas such as the sunrise view (Figure 66)



Figure 66 Sunrise View

## References

---

- [1] D. A. Simon and S. Lavalley, "Medical imaging and registration in computer assisted surgery," *Clinical Orthopaedics and Related Research*, pp. 17-27, Sep 1998.
- [2] K. Burckhardt, C. Gerber, J. Hodler, H. Nötzli, and G. Székely, "Precision of distance determination using 3D to 2D projections: The error of migration measurement using X-ray images," *Medical Image Analysis*, vol. 4, pp. 375-388, 2000.
- [3] J. Kim, T. Park, S. Park, I. Kim, and S. Kim, "Measurement of femoral neck anteversion in 3D. Part 1: 3D imaging method," *Medical and Biological Engineering and Computing*, vol. 38, pp. 603-609, 2000.
- [4] H. Watch. (2008, March 24) Health Watch. *US News & World Report*. 66.
- [5] S. Kurtz, K. Ong, E. Lau, F. Mowat, and M. Halpern, "Projections of Primary and Revision Hip and Knee Arthroplasty in the United States from 2005 to 2030," *The Journal of Bone & Joint Surgery*, vol. 89, pp. 780-785, 2007.
- [6] A. Le Bras, S. Laporte, V. Bousson, D. Mitton, J. A. De Guise, J. D. Laredo, *et al.*, "3D reconstruction of the proximal femur with low-dose digital stereoradiography," *Comput Aided Surg*, vol. 9, pp. 51-7, 2004.
- [7] S. Laporte, W. Skalli, J. A. de Guise, F. Lavaste, and D. Mitton, "A biplanar reconstruction method based on 2D and 3D contours: application to the distal femur," *Computer Methods in Biomechanics and Biomedical Engineering*, vol. 6, pp. 1-6, Feb 2003.
- [8] P. Gamage, S. Q. Xie, P. Delmas, and W. L. Xu, "Diagnostic radiograph based 3D bone reconstruction framework: Application to the femur," *Computerized Medical Imaging and Graphics*, vol. 35, pp. 427-437, 9// 2011.
- [9] C. Langton, S. Pisharody, and J. Keyak, "Generation of a 3D proximal femur shape from a single projection 2D radiographic image," *Osteoporosis International*, vol. 20, pp. 455-461, 2009.
- [10] S. Benameur, M. Mignotte, S. Parent, H. Labelle, W. Skalli, and J. de Guise, "3D/2D registration and segmentation of scoliotic vertebrae using statistical models," *Computerized Medical Imaging and Graphics*, vol. 27, pp. 321-337, 2003.
- [11] G. Zheng, S. Gollmer, S. Schumann, X. Dong, T. Feilkas, and M. A. González Ballester, "A 2D/3D correspondence building method for reconstruction of a patient-specific 3D bone surface model using point distribution models and calibrated X-ray images," *Medical Image Analysis*, vol. 13, pp. 883-899, 2009 2009.
- [12] N. Baka, B. L. Kaptein, M. de Bruijne, T. van Walsum, J. E. Giphart, W. J. Niessen, *et al.*, "2D-3D shape reconstruction of the distal femur from stereo X-ray imaging using statistical shape models," *Medical Image Analysis*, vol. 15, pp. 840-850, 2011.
- [13] T. F. Cootes, C. J. Taylor, D. H. Cooper, and J. Graham, "Active Shape Models-Their Training and Application," *Computer Vision and Image Understanding*, vol. 61, pp. 38-59, 1995.
- [14] S. Benameur, M. Mignotte, F. Destrepes, and J. A. De Guise, "Three-Dimensional Biplanar Reconstruction of Scoliotic Rib Cage Using the Estimation of a Mixture of Probabilistic Prior Models  
" *IEEE Transactions on Biomedical Engineering*, vol. 52, October 2005 2005.
- [15] T. Cresson, B. Godbout, D. Branchaud, R. Chav, P. Gravel, and J. A. De Guise, "Surface reconstruction from planar x-ray images using moving least squares," in *Engineering*

- in Medicine and Biology Society, 2008. EMBS 2008. 30th Annual International Conference of the IEEE, 2008, pp. 3967-3970.*
- [16] J. Canny, "A Computational Approach to Edge Detection," *Pattern Analysis and Machine Intelligence, IEEE Transactions on*, vol. PAMI-8, pp. 679-698, 1986.
- [17] D. Xiao and Z. Guoyan, "Determining Geometrical Parameters by Particle Filter for Automatic Reconstruction of Surface Model of Proximal Femur from Biplanar Calibrated Fluoroscopic Images," in *Control, Automation, Robotics and Vision, 2006. ICARCV '06. 9th International Conference on*, 2006, pp. 1-6.
- [18] M. Fleute and S. Lavallée, "Nonrigid 3-D/2-D Registration of Images Using Statistical Models  
Medical Image Computing and Computer-Assisted Intervention – MICCAI'99." vol. 1679, C. Taylor and A. Colchester, Eds., ed: Springer Berlin / Heidelberg, 1999, pp. 138-147.
- [19] A. Gueziec, P. Kazanzides, B. Williamson, and R. H. Taylor, "Anatomy-based registration of CT-scan and intraoperative X-ray images for guiding a surgical robot," *Medical Imaging, IEEE Transactions on*, vol. 17, pp. 715-728, 1998.
- [20] D. Mitton, S. Deschânes, S. Laporte, B. Godbout, S. Bertrand, J. A. De Guise, *et al.*, "3D reconstruction of the pelvis from bi-planar radiography," in *Computer Methods in Biomechanics & Biomedical Engineering* vol. 9, ed: Taylor & Francis Ltd, 2006, pp. 1-5.
- [21] S. Kolta, A. Le Bras, D. Mitton, V. Bousson, J. A. de Guise, J. Fechtenbaum, *et al.*, "Three-dimensional X-ray absorptiometry (3D-XA): a method for reconstruction of human bones using a dual X-ray absorptiometry device," *Osteoporosis International*, vol. 16, pp. 969-976, 2005.
- [22] S. Kolta, S. Quiligotti, A. Ruyssen-Witrand, A. Amido, D. Mitton, A. L. Bras, *et al.*, "In vivo 3D reconstruction of human vertebrae with the three-dimensional X-ray absorptiometry (3D-XA) method," *Osteoporos Int*, vol. 19, pp. 185-92, Feb 2008.
- [23] M. A. Oliver and R. Webster, "Kriging: a Method of Interpolation for Geographical Information Systems " *Int. J. Geographic Information Systems* vol. 4, pp. 313-332 1990.
- [24] G. Celeux and J. Diebolt, "The SEM algorithm: A probabilistic teacher algorithm derived from the EM algorithm for the mixture problem," *Computational Statist. Quart.* , vol. 2, pp. 73-82 1985
- [25] S. Lavallee and R. Szeliski, "Recovering the position and orientation of free-form objects from image contours using 3D distance maps," *IEEE transactions on pattern analysis and machine intelligence*, vol. 17, 1995.
- [26] M. R. Mahfouz, W. A. Hoff, R. D. Komistek, and D. A. Dennis, "A robust method for registration of three-dimensional knee implant models to two-dimensional fluoroscopy images," *Medical Imaging, IEEE Transactions on*, vol. 22, pp. 1561-1574, 2003.
- [27] S. Benameur, M. Mignotte, S. Parent, H. Labelle, W. Skalli, and J. A. De Guise, "3D biplanar reconstruction of scoliotic vertebrae using statistical models," in *Computer Vision and Pattern Recognition, 2001. CVPR 2001. Proceedings of the 2001 IEEE Computer Society Conference on*, 2001, pp. II-577-II-582 vol.2.

- [28] J. Tohka, "Global optimization of deformable surface meshes based on genetic algorithms," in *Image Analysis and Processing, 2001. Proceedings. 11th International Conference on*, 2001, pp. 459-464.
- [29] G. Zheng, "Statistical Deformable Model-Based Reconstruction of a Patient-Specific Surface Model from Single Standard X-ray Radiograph," in *Computer Analysis of Images and Patterns*. vol. 5702, X. Jiang and N. Petkov, Eds., ed: Springer Berlin Heidelberg, 2009, pp. 672-679.
- [30] E. E. A. Fatah, M. Mahfouz, and H. E. Dakhakhni, "Analysis of variation and automated measurement of adult proximal femora using sex-specific atlases," presented at the 8th International Symposium on Computer Methods in Biomechanics and Biomedical Engineering, Portugal, 2008.
- [31] M. R. Mahfouz, B. C. Merkl, E. E. Fatah, R. J. Booth, and J. N. Argenson, "Automatic methods for characterization of sexual dimorphism of adult femora: distal femur.," *Computer Methods in Biomechanics and Biomedical Engineering*, vol. 10, pp. 447-456, 2007.
- [32] A. D. Nguyen and S. J. Shultz, "Sex differences in clinical measures of lower extremity alignment," *The Journal of orthopaedic and sports physical therapy*, vol. 37, pp. 389-398, 07/ 2007.
- [33] K. S. Arun, T. S. Huang, and S. D. Blostein, "Least-squares fitting of two 3-D point sets," *IEEE Trans. Pattern Anal. Mach. Intell.*, vol. 9, pp. 698-700, 1987.
- [34] I. T. Jolliffe, *Principal Component Analysis*: Springer, 2002.
- [35] A. Savitzky and M. J. E. Golay, "Smoothing and Differentiation of Data by Simplified Least Squares Procedures," *Analytical Chemistry*, vol. 36, pp. 1627-1639, 1964/07/01 1964.
- [36] W. Eric and L. Grimson, *Object recognition by computer: the role of geometric constraints*: MIT Press, 1990.
- [37] A. Sherrod and W. Jones, Eds., *Beginning DirectX 11 Game Programming*. Course Technology Press, 2011, p.^pp. Pages.
- [38] D. Shreiner, Ed., *OpenGL Programming Guide: The Official Guide to Learning OpenGL, Versions 3.0 and 3.1*. Addison-Wesley Professional 2009, p.^pp. Pages.
- [39] NVIDIA. <http://www.nvidia.com>.
- [40] AMD, "<http://www.amd.com/us/products/Pages/graphics.aspx>."
- [41] E. Trucco and A. Verri, *Introductory Techniques for 3-D Computer Vision*: Prentice Hall, 1998.
- [42] M. J. D. Powell, "An efficient method for finding the minimum of a function of several variables without calculating derivatives," *The Computer Journal*, vol. 7, pp. 155-162, January 1, 1964 1964.
- [43] D. F. Dementhon and L. S. Davis, "Model-based object pose in 25 lines of code," *International Journal of Computer Vision*, vol. 15, pp. 123-141, 1995.
- [44] M. A. Fischler and R. C. Bolles, "Random sample consensus: a paradigm for model fitting with applications to image analysis and automated cartography," *Commun. ACM*, vol. 24, pp. 381-395, 1981.
- [45] P. J. van Otterloo, *A Contour-Oriented Approach to Shape Analysis*: Prentice Hall, 1991.

- [46] D. Zhang and G. Lu, "A Comparative Study on Shape Retrieval Using Fourier Descriptors with Different Shape Signatures," *Journal of Visual Communication and Image Representation*, pp. 41-60, 2003.
- [47] M. B. Stegmann and Danmarks Tekniske Universitet. Institut for Matematisk Modellering, *Active appearance models : theory extensions and cases*. Lyngby: Institut for Matematisk Modellering, Danmarks Tekniske Universitet, 2000.
- [48] F. Mokhtarian and M. Bober, *Curvature Scale Space Representation: Theory, Applications, and MPEG-7 Standardization*: Kluwer Academic Publishers, 2003.
- [49] L. Shamir, S. M. Ling, W. W. Scott, Jr., A. Bos, N. Orlov, T. J. Macura, *et al.*, "Knee x-ray image analysis method for automated detection of osteoarthritis," *IEEE Trans Biomed Eng*, vol. 56, pp. 407-15, Feb 2009.
- [50] H. Stark, *Image recovery: Theory and application*: Academic Press, 1987.
- [51] P. A. Jansson, *Deconvolution of images and spectra*, 2 ed.: Academic Press, Inc., 1996.
- [52] R. J. Marks II "Alternating Projections onto Convex Sets " in *Deconvolution of Images and Spectra* P. A. Jansson, Ed., ed San Diego Academic Press, 1997, pp. 476-501.
- [53] M. Johnson, "Analysis, Segmentation and Prediction of Knee Cartilage using Statistical Shape Models," PhD, Mechanical, Aerospace, and Biomedical Engineering, University of Tennessee, 2013.
- [54] H. Livyatan, Z. Yaniv, and L. Joskowicz, "Gradient-based 2-D/3-D rigid registration of fluoroscopic X-ray to CT," *Medical Imaging, IEEE Transactions on*, vol. 22, pp. 1395-1406, 2003.

## Vita

---



Hatem Amin El Dakhakhni was born in Cairo, Egypt in 1980. He received a B.S. degree in Biomedical Engineering from Cairo University in 2002 and a M.S. degree in Biomedical Engineering from the University of Tennessee, Knoxville, TN, USA in 2008. He received the Ph.D. degree in Biomedical Engineering from the University of Tennessee, Knoxville, TN, USA in 2013. He is currently a Biomedical Engineering Consultant at Techmah LLC, based in Knoxville, TN, USA. His current research interests include medical imaging, 2D and 3D visualization, statistical modeling, and orthopedic design.